

Cored DARKexp systems with finite size: numerical results

Claudio Destri

Dipartimento di Fisica G. Occhialini, Università Milano-Bicocca
and INFN, sezione di Milano-Bicocca, Piazza della Scienza 3, 20126 Milano, Italia.

E-mail: claudio.destri@mib.infn.it

Abstract. In the DARKexp framework for collisionless isotropic relaxation of self-gravitating matter, the central object is the differential energy distribution $n(E)$, which takes a maximum-entropy form proportional to $\exp[-\beta(E - \Phi(0))] - 1$, $\Phi(0)$ being the depth of the potential well and β the standard Lagrange multiplier. Then the first and quite non-trivial problem consists in the determination of an ergodic phase-space distribution which reproduces this $n(E)$. In this work we present a very extensive and accurate numerical solution of such DARKexp problem for systems with cored mass density and finite size. This solution holds throughout the energy interval $\Phi(0) \leq E \leq 0$ and is double-valued for a certain interval of β . The size of the system represents a unique identifier for each member of this solution family and diverges as β approaches a specific value. In this limit, the tail of the mass density $\rho(r)$ dies off as r^{-4} , while at small radii it always starts off linearly in r , that is $\rho(r) - \rho(0) \propto r$.

Contents

1	Introduction and summary	1
2	Dimensionless formulation for cored DARKexp systems	4
2.1	The case of infinite size	8
2.2	About energies	8
3	Analytic results	10
4	Numerical approach	11
4.1	Integral transforms and Poisson’s equation	12
4.2	System of non-linear equations	14
5	Numerical results	15
5.1	Solutions of the first kind	17
5.2	Solutions of the second kind	21
5.3	A unifying view of the two kinds of solutions	25
5.4	Asymptotic fit	27
6	Discussion and outlook	28
A	Accuracy checks and algorithmic details	29

1 Introduction and summary

One of the long-lasting question in statistical physics concerns the equilibrium, or *quasi*-equilibrium in collisionless self-gravitating systems. In the limit of continuous matter, the dynamics in such systems is well described in the single particle phase-space by the Vlasov-Poisson (or collisionless Boltzmann) equation [1, 2]. But this equation retains full memory of the initial conditions at the fine-grained level. Yet observations and N -body simulations show that collisionless systems of many different kinds and sizes appear, at the coarse-grained level, to be in very similar quasi-stationary states [3–6].

This fact naturally suggests that some sort of maximum-entropy principle should be at work also for the outcome of collisionless gravitational collapses, and many proposals in this direction have been put forward throughout the years ([7–16] is a very incomplete list), although no general framework or specific model has yet obtained the success and recognition that standard Gibbs-Maxwell-Boltzmann equilibrium enjoys for systems with short-range interactions.

Apart from well-known intrinsic theoretical difficulties, one reason for this unsatisfactory state of the art lays in the many limitations and subtleties that dominate the scene when observations are compared with N -body simulations and both are contrasted with first-principle theoretical models. First of all, astrophysical observations have a well-known limited discriminating power and very often the data themselves depend on more or less arbitrary assumptions on the underlying dynamics. Secondly, even when we are convinced to be dealing with purely self-gravitating matter in a collisionless regime, such as with dark matter, it is not

easy to disentangle a localized gravitational collapse from all the rest. In dark-matter-driven cosmological structure formation there are hierarchical collapses, filaments, mergers, tidal strippings and other complex effects that make it difficult to unambiguously identify relaxed outcomes of well defined collapses. When eventually well-localized quasi-stationary systems emerge, such as galaxies, baryons with their complicated non-gravitational interactions could play a role also in the shaping of the inner part of the dark matter halo that hosts a visible galaxy [17–21]. Furthermore, given that we only have an indirect knowledge of DM, we cannot apriori exclude the possibility of a self-interacting DM whose elastic collisions could significantly alter the collisionless density profiles observed in N -body simulations [22–26]. Another possibility is to vary the initial conditions of structure formation and in particular the dispersion velocity of the hypothetical DM particles; this could very well affect also the outcomes of localized small-scale collapses. Cold DM suffers from the so-called small-scale crisis, as it yields too much structure at small scales and cuspy density profiles à la Navarro–Frenk–White. Warm DM avoids the small scale overabundance [27, 28] (but perhaps entering in conflict with Lyman- α observation data [29]) and is expected to yield cored profiles [30–34], although probably too small to reconcile N -body simulations with observations without the help of baryonic feed-back [34–36]. If DM is warm, even Quantum Mechanics might play a role in the quasi-equilibrium of small dwarf galaxies [37, 38], which are the systems where observations and pure CDM N -body simulations disagree the most. And certainly this is only a partial list of possibilities.

For this reason, in our opinion a practical and effective approach to the theoretical problem should start by clearly delimiting the scope of the investigation, leaving possible applications, with all the necessary provisos and adjustments, to a second stage, but dealing with the theory, whether analytically or numerically, as carefully as possible. This is the framework we choose for the present work.

There are two fundamental prerequisites that any maximum-entropy model of the collisionless collapse ought to satisfy: the system should be in dynamical equilibrium, that is the phase-space mass distribution should be a function of the isolating integrals of the motion, and it should have finite mass and energy. One such model is the DARKexp model, originally put forward by Hjorth and Williams in [14] with the explicit purpose of providing a statistical-mechanical basis for the Navarro–Frenk–White density profile [39]. In its simplest version, which applies to fully isotropic systems, the model envisage an ergodic phase-space mass distribution f that depends only on the orbit energy $E = \frac{1}{2}v^2 + \Phi$, with $\Phi(r)$ the spherically symmetric gravitational potential, just as many other well-known models [3]. The crucial difference w.r.t. to other maximum-entropy formulations, such as the isothermal sphere, is that the maximization of Boltzmann–Shannon entropy is assumed in energy space rather than in phase space (see [14] for the motivations). Moreover, the small occupation numbers of energy states close to the bottom of the potential well is estimated more accurately than with the Stirling approximation, as done for instance in finite-mass collisional systems near the escape energy [40]. It follows that only the differential energy distribution $n(E)$ [3] is explicitly derived in the DARKexp model and reads

$$n(E) \propto \exp[-\beta(E - \Phi(0))] - 1, \quad (1.1)$$

where β is a Lagrange multiplier that fixes the mean energy of the system, while the overall normalization is fixed by the total mass. Clearly, by construction, a DARKexp systems has a finite mass and a finite energy. The phase-space mass distribution $f(E)$, and with it all physical observables such as the mass density $\rho(r)$ and the velocity dispersion $\sigma(r)$, must

be computed from $n(E)$. This is a highly non-trivial task, which is formulated in detail in section 2, since the $n(E)$ to $f(E)$ relation depends on the potential $\Phi(r)$, that is not known a priori. Eventually, the reconstructed DARKexp $\rho(r)$ and $\Phi(r)$ depend on three free parameters: the two arbitrary scales in mass and distances (the third scale is fixed by Newton's constant) and a dimensionless shape parameter related to β . A fundamental analytic property of the DARKexp setup was highlighted in [14]: if $\rho(r)$ has the a $1/r$ cusp as $r \rightarrow 0$, then $f(E) \sim (E - \Phi(0))^{-5/2}$, $\Phi(r) - \phi(0) \sim r$ and $g(E) \sim (E - \Phi(0))^{7/2}$ as $E \rightarrow \Phi(0)$, so that $n(E) \sim E - \Phi(0)$ in agreement with eq. (1.1).

Strictly speaking, the DARKexp framework just introduced has a logical loophole if it is meant solely as a statistical-mechanical foundation to NFW $1/r$ profile, the prototype of the cuspy profiles characteristic of pure CDM N -body simulations. In fact, DARKexp deals with continuous matter and therefore it applies to the realistic collapse of DM particles of arbitrary mass (as long as their number in any resolvable volume is large enough to neglect the collisional dissipation). And yet, it is known that the primordial DM velocity dispersion, which strongly depends on the DM particle mass, has a direct effect on the inner profile of relaxed halos. In other words, DARKexp would predict $1/r$ cusps also for relaxed WDM, which instead features cores, albeit apparently not large enough to agree with observations. Therefore, it is reasonable to investigate also the possibility of DARKexp cored systems and to justify the use of the DARKexp model more on its acceptable consistency with observations and N -body simulation than on its implication of $1/r$ cusps.

Indeed, the DARKexp model has been tested against observations and/or N -body simulations in two distinct ways: in [41, 42] the $n(E)$ of eq. (1.1) was compared to the differential energy distribution extracted from N -body simulations. In [42–44] the mass density implied by $n(E)$ (and numerically computed) was directly compared to observations and/or N -body simulations. In both cases the DARKexp model fares quite well. However, in both cases there are obvious limitations to the finite resolving power, either for energies very close to the potential depth or for very small spatial distances from the center of mass. Similarly, there are limitations near the escape energy or at large distances. The situation becomes even more involved in the case of the DARKexp $\rho(r)$, since it has to be computed numerically from $n(E)$ and it may suffer itself from limitations at small and large distances. This is the case for the numerical method just mentioned in [45] and briefly described on [43], which is originally due to Binney [46] and is affected by numerical instabilities at distances too small or too large. Moreover, this recursive method might very well suffer also from numerical artifacts even where it appears to be stable, especially if the mass density $\rho(r)$ blows up when $r \rightarrow 0$ as in the case of the NFW profile. The density profiles and their logarithmic slopes plotted in Figs. 1 and 2 of [45] do show peculiar oscillations that give no hint to settle on the $r \rightarrow 0$ asymptotics of NFW profile, which is nonetheless claimed to be a consequence of the DARKexp model. Apparently, this is not a problem for the good fit to observations and N -body simulations, since this is confined to a region where the oscillations are negligible, but it does make the basis of the DARKexp model less firm than it is reasonable to accept.

With the motivation of clarifying the $n(E)$ to $\rho(r)$ relation of the DARKexp model, in [47] we performed a next-to-leading asymptotic analysis when the leading behavior of $\rho(r)$ is assumed to be the cuspy one of the NFW profile or just a standard core like in most ergodic systems. In fact, contrary to some common lore, in [47] it was shown that cored profiles are perfectly consistent with a $n(E)$ linearly vanishing when $E \rightarrow \Phi(0)$ as in eq. (1.1). Furthermore, it was shown that the next-to-leading asymptotics in the case of cores is much

better behaved than in the case of $1/r$ -cusps. In the present work we complete the analysis in the case of cored systems with a finite size by computing very accurate numerical solutions of the DARKexp problem that perfectly match the asymptotic behavior analytically determined in [47]. In other words, we obtain the profiles for $f(E)$ and $\rho(r)$ at many different values of β with no limitations on the range of E or r . In particular, this means that our numerical solutions confirm the behavior of $\rho(r)$ near $r = 0$ reported in eq. 7.2 of [47], namely

$$\rho(r) \simeq \rho_0 \left[1 + \gamma_0 r - \frac{32}{5\pi^2} \gamma_0^2 r^2 \log r + O(r^2) \right],$$

where ρ_0 and γ_0 represent the two free scales of the problem.

Our numerical approach is described in detail in section 4. It is based on the precise dimensionless formulation of the DARKexp problem put forward in [47] and repeated here in section 2 for completeness. This formulation lends itself very naturally to the use of the Chebyshev approximation as central numerical tool. The results are described in detail in section 5. A quick summary is provided by Figs. 14 and 15, where we plot the mass density profiles, their logarithmic slopes and the velocity dispersions. The density and its logarithmic slope are always monotonic. For obvious reasons in these figures the logarithm of radial coordinate is bound on the left, but our numerical approach is capable of computing $\rho(r)$ with $O(10^{-10})$ accuracy for any value of r , no matter how small.

Another prominent and somewhat unexpected feature is the dependence of the DARKexp solutions on the Lagrange multiplier β , which plays a role similar to that of a negative inverse temperature. This behavior turns out to be double-valued, with an upper limit on β in one of the two determinations, as summarized in Fig. 12 (b is a dimensionless variable proportional to β).

Altogether, the cored DARKexp systems with finite size that we have computed represent an interesting family of ergodic self-gravitating systems, regardless of their probably limited applicability to actual physical situations. They range from very compact and hot, almost uniform spheres, to cold and diffused halos with a r^{-4} tail that eventually drops to zero arbitrarily far away from the origin, since the size of the system diverges when β tends to a specific limiting value. Let us recall that we are dealing here with continuous ergodic systems that are completely relaxed in energy. In real gravitational collapses, for instance of DM, even assuming perfect spherical symmetry there remains the magnitude of angular momentum as isolating integral of the motion, which is connected to the velocity anisotropy. Indeed the DM halos in N -body simulations have a characteristic non-zero anisotropy $\beta(r)$. In [41] it was argued that if DARKexp halos had similar $\beta(r)$, their density and energy distributions could not be distinguished from those of isotropic DARKexp halos. This line of argument was further developed in [48], where the role of angular momentum in the DARKexp maximum-entropy setup was carefully studied with a mixed theoretical and phenomenological approach. In both cases the DARKexp $n(E)$ was regarded as implying a $1/r$ -cusped density with effectively unlimited support. It should be interesting to extend this kind of analysis to the cored DARKexp systems with finite size presented here.

2 Dimensionless formulation for cored DARKexp systems

A spherically symmetric system is characterized by the Poisson's equation

$$\phi'' + \frac{2}{r}\phi' = 4\pi G\rho. \quad (2.1)$$

Here we assume that the mass density $\rho = \rho(r)$ is finite at $r = 0$, yields a finite total mass M and vanishes when $r \geq r_0$ for some r_0 , possibly infinite, that defines the size of the system. We then fix the arbitrary constant mode of the gravitational potential ϕ by demanding that $\phi(r_0) = 0$. By Gauss law ϕ is monotonically increasing in r and so $\phi(r) < 0 (> 0)$ for $r < r_0 (> r_0)$ with $\lim_{r \rightarrow \infty} \phi(r) = GM/r_0$.

Choosing units such that $4\pi G = 1$, there remain two arbitrary scales for eq. (2.1), which can be fixed in terms of $\rho_0 = \rho(0)$ and $\phi_0 = \phi(0)$. Hence we can set

$$\rho(r) = \frac{1}{3}\rho_0 \nu(u(x)), \quad \phi(r) = \phi_0[1 - u(x)], \quad x \equiv \frac{r}{r_*}, \quad r_*^2 = \frac{3|\phi_0|}{\rho_0},$$

where $\nu(u)$ and $u(x)$ are dimensionless functions of their own dimensionless argument and $u(x)$ monotonically grows from 0 to 1 as x grows from 0 to r_0/r_* . By construction $\nu(0) = 3$ and Poisson's equation now reads

$$u''(x) + \frac{2}{x}u'(x) = \nu(u(x)). \quad (2.2)$$

while the solution must behave as $u \simeq \frac{1}{2}x^2$ when $x \rightarrow 0$.

The monotonic relation between x and u also allows to rewrite eq. (2.2) as

$$\frac{2}{x(u)x'(u)} - \frac{x''(u)}{[x'(u)]^3} = \nu(u), \quad (2.3)$$

with $x \simeq (2u)^{1/2}$ as $u \rightarrow 0$. Notice that in this last reformulation of Poisson's equation the non-linearity is fixed independently of the form of $\nu(u)$ and the domain of the now independent variable u is fixed once and for all to $[0, 1]$, with the system bounded whenever $x(1) = r_0/r_*$ is finite. On the other hand, eq. (2.3) hides an important positivity property of Poisson's equation which is instead manifest in eq. (2.2), since this is equivalent to the integral equation

$$u(x) = \int_0^x dy y^{-2} \int_0^y dz z^2 \nu(u(z)) = \int_0^x dy y^2 (y^{-1} - x^{-1}) \nu(u(y)). \quad (2.4)$$

We can see that any variation of $\nu(u)$ with a definite sign implies a variation of $u(x)$ with the same sign and therefore a variation of $x(u)$ with the opposite sign.

In its simplest version, the DARKexp model describes isotropic systems with an ergodic phase-space mass distribution $f = f(\frac{1}{2}v^2 + \phi(r))$, from which ρ is recovered as

$$\begin{aligned} \rho(r) &= \int d^3v f(\frac{1}{2}v^2 + \phi(r)) = \int dE f(E) \int d^3v \delta(\frac{1}{2}v^2 + \phi(r) - E) \\ &= 4\pi \int_{\phi(r)}^0 dE f(E) [2(E - \phi(r))]^{1/2}. \end{aligned} \quad (2.5)$$

Here we have used that $f(E) = 0$ for $E > 0$ as dictated by the condition of bound matter with finite total mass. If we parametrize the one-particle energy as the potential, that is

$$E = \phi_0(1 - s), \quad 0 \leq s \leq 1, \quad (2.6)$$

then we can write

$$f(E) = \frac{(2|\phi_0|)^{-1/2}}{4\pi r_*^2} F(s),$$

with $F(s)$ dimensionless and

$$\nu(u) = \int_u^1 ds F(s) (s - u)^{1/2} . \quad (2.7)$$

This integral transform is the half-primitive of $F(s)$ vanishing at $s = 1$ and can be inverted into the half-derivative

$$F(s) = \frac{2}{\pi} \frac{d}{ds} \int_s^1 du \nu'(u) (u - s)^{-1/2} . \quad (2.8)$$

The differential energy distribution [3] reads

$$n(E) = \frac{dM}{dE} = \int d^3r \int d^3v f(\frac{1}{2}v^2 + \phi(r)) \delta(\frac{1}{2}v^2 + \phi(r) - E) = f(E)g(E) ,$$

where $g(E)$ is the density of states at a given one-particle energy E ,

$$g(E) = \int d^3r \int d^3v \delta(\frac{1}{2}v^2 + \phi(r) - E) = (4\pi)^2 \int_0^{r_E} dr r^2 [2(E - \phi(r))]^{1/2} \quad (2.9)$$

and r_E is the radius where the one-particle kinetic energy vanishes, that is $E = \phi(r_E)$. By definition we have

$$M = \int_{\phi_0}^0 dE n(E) . \quad (2.10)$$

In dimensionless terms

$$M = 4\pi r_* |\phi_0| m = \frac{4\pi}{3} \rho_0 r_*^3 m , \quad m = \int_0^1 du x^2(u) x'(u) \nu(u) \quad (2.11)$$

and

$$n(E) = 4\pi r_* N(s) , \quad g(E) = (4\pi)^2 r_*^3 (2|\phi_0|)^{1/2} G(s) ,$$

where

$$N(s) = F(s)G(s) , \quad \int_0^1 ds N(s) = m$$

and

$$G(s) = \int_0^s du x^2(u) x'(u) (s - u)^{1/2} = \frac{1}{6} \int_0^s du x^3(u) (s - u)^{-1/2} , \quad (2.12)$$

This integral transform (the half-primitive of $x^2(u)x'(u)$ vanishing at $s = 0$) can be inverted as

$$x^3(u) = \frac{6}{\pi} \int_0^u ds G'(s) (u - s)^{-1/2} . \quad (2.13)$$

Altogether the four functions F , ν , x and G are connected as follows

$$F(s) \begin{array}{c} \xrightarrow{\text{eq. (2.7)}} \\ \xleftarrow{\text{eq. (2.8)}} \end{array} \nu(u) \begin{array}{c} \xrightarrow{\text{eq. (2.3)}} \\ \xleftarrow{\text{eq. (2.3)}} \end{array} x(u) \begin{array}{c} \xrightarrow{\text{eq. (2.12)}} \\ \xleftarrow{\text{eq. (2.13)}} \end{array} G(s) . \quad (2.14)$$

and the central problem of any approach in which $n(E)$ is given beforehand, is to find functions F and G such that $F(s)G(s) = N(s)$, taking into account that by eq. (2.14) F and G

are complicated non-local and non-linear functionals one of the other. In particular, the DARKexp differential energy distribution has the form

$$n(E) = C \{ \exp[-\beta(E - \phi_0)] - 1 \} \quad , \quad \phi_0 \leq E \leq 0 \quad ,$$

where the two dimension-full constants C and β act as Lagrange multipliers that fix the total mass and the average one-particle energy, respectively. In the present dimensionless setup, we set

$$b = \beta\phi_0 \quad , \quad C' = \frac{C}{4\pi r_*}$$

so that

$$N(s) = F(s)G(s) = C' (e^{bs} - 1) = \frac{mb}{e^b - 1 - b} (e^{bs} - 1) \quad , \quad (2.15)$$

where the last equality, fixing C' , ensures that $\int_0^1 ds N(s) = m$, while the dimensionless parameter b relates to the average value of the one-particle energy, $\bar{E} = \phi_0(1 - \bar{s})$, through

$$\bar{s} = \frac{\int_0^1 ds s (e^{bs} - 1)}{\int_0^1 ds (e^{bs} - 1)} = \frac{(b-1)e^b + 1 - b^2/2}{b(e^b - 1 - b)} \quad . \quad (2.16)$$

$N(s)$ is positive-defined, as necessary, both for $b < 0$ and $b > 0$. In both cases it is also monotonically increasing in s , that is in the one-particle energy E . On the other hand, $N(s)$ is convex for $b > 0$ and concave for $b < 0$, while it reduces to a linear ramp for $b = 0$. As b ranges from $-\infty$ to $+\infty$, \bar{s} monotonically grows from $1/2$ to 1 , so that a solution for b exists only for $\bar{s} > 1/2$ and is unique. Moreover, $b(\bar{s})$ is negative for $1/2 < \bar{s} < 2/3$ and positive for $\bar{s} > 2/3$.

Eq. (2.15) implies that $F(s)G(s) \sim s$ as $s \rightarrow 0$. Since $x \simeq (2u)^{1/2}$ as $u \rightarrow 0$, we have

$$G(s) \simeq \frac{1}{4\sqrt{2}} \pi s^2 \quad , \quad (2.17)$$

where we used the definition of Euler's Beta function

$$\int_0^s du u^{z-1} (s-u)^{w-1} = B(z, w) s^{z+w-1}$$

along with $B(\frac{3}{2}, \frac{3}{2}) = \frac{1}{8}\pi$. Hence

$$F(s) \simeq K s^{-1} \quad , \quad (2.18)$$

for some constant K to be determined. When $u = 0$, the $s^{-1/2}$ singularity in the integrand of eq. (2.7) is integrable, hence all values of $F(s)$ over the range $0 \leq s \leq 1$ contribute to $\nu(0) = 3$ and K cannot be determined without solving the full problem. To this end, it is convenient to set

$$F(s) = K s^{-1} (1 - hs)^{5/2} \xi_F(s) \quad (2.19)$$

and

$$G(s) = 2^{-5/2} \pi s^2 (1 - hs)^{-5/2} \xi_G(s) \quad , \quad (2.20)$$

where h is a free parameter, with $0 \leq h \leq 1$. The reason for this peculiar parametrization will become clear later on. Now the problem $F(s)G(s) = N(s)$ takes the form

$$\xi_F(s)\xi_G(s) = A(bs) \quad , \quad A(z) \equiv \frac{e^z - 1}{z} \quad (2.21)$$

while

$$K = \frac{3}{\int_0^1 ds (1 - hs)^{5/2} \xi_F(s) s^{-1/2}}, \quad m = 2^{-5/2} \pi K \frac{e^b - 1 - b}{b^2}; \quad (2.22)$$

A more comprehensive notation, highlighting all dependencies on the dimensionless variables s , b and h as well as the functional dependence of G on F through the chain (2.14), would be

$$F(s, b) = K(b) s^{-1} (1 - hs)^{5/2} \xi_F(s, b, h),$$

$$G(s, b; [F]) = 2^{-5/2} \pi s^2 (1 - hs)^{-5/2} \xi_G(s, b, h, [\xi_F]),$$

and

$$\xi_F(s, b, h) \xi_G(s, b, h, [\xi_F]) = A(bs),$$

but we will stick to the shorter notation used before, for the sake of brevity. It should be noted, however, that ξ_F and ξ_G , and therefore also K and m , could multi-valued as functions of b in case the solution of eq. (2.21) is not unique. Notice also that, by construction, $\xi_F(0) \xi_G(0) = A(0)$ identically.

2.1 The case of infinite size

The size of the system is given by $r_* x(1)$ and it could be infinite. That is to say, for certain values of b the solution of eq. (2.21) might be such that $\xi_F(1) = 0$ and $\lim_{s \rightarrow 1} \xi_x(1) = \lim_{s \rightarrow 1} \xi_G(s) = +\infty$. In fact, a finite mass system always has a Newtonian potential dying off at infinity as GM/r . Hence, if $\lim_{u \rightarrow 1} x(u) = +\infty$, it must be as a pole of order one, since

$$\lim_{u \rightarrow 1} (1 - u)x(u) = m.$$

Then, by eq. (2.12), $G(s)$ must diverge at $s = 1$ as $(1 - s)^{-5/2}$ [see few lines below eq. (4.9) for a rigorous derivation], which in turn implies that $F(s)$ must vanish there as $(1 - s)^{5/2}$ [so that $\nu(u)$ dies as $(1 - u)^4$ at $u = 1$, or $\rho(r) \sim r^{-4}$ as $r \rightarrow \infty$]. This fact explain our peculiar parametrization in eqs. (2.19) and (2.20), which allows, by letting $h \rightarrow 1$, to keep $\xi_G(s)$ a bounded function over the unit interval $[0, 1]$, which is much easier to handle numerically. As a matter of fact, this parametrization is numerically very convenient also for systems with finite but very large size, since h can be tuned to keep $\xi_G(1)$ relatively small when $G(1)$ becomes very large.

2.2 About energies

A system described by the ergodic phase-space mass distribution $f(E)$ is isotropic, with the squared velocity dispersion given by

$$\sigma^2(r) = \frac{1}{\rho(r)} \int d^3v v^2 f(\frac{1}{2}v^2 + \phi(r)) = \frac{4\pi}{\rho(r)} \int_{\phi(r)}^0 dE f(E) [2(E - \phi(r))]^{3/2}. \quad (2.23)$$

Hence the total kinetic energy reads

$$\mathcal{K} = \frac{1}{2} \int d^3r \rho(r) \sigma^2(r) = \frac{1}{2} \int_{\phi_0}^0 dE f(E) g_3(E),$$

where (recall that $E = \phi(r_E)$)

$$g_3(E) = (4\pi)^2 \int_0^{r_E} dr r^2 [2(E - \phi(r))]^{3/2} = (4\pi)^2 \int_0^{r_E} dr r^3 \phi'(r) [2(E - \phi(r))]^{1/2}. \quad (2.24)$$

The total potential energy reads

$$\mathcal{U} = - \int d^3r \rho \mathbf{r} \cdot \nabla \phi = -4\pi \int_0^{r_0} dr r^3 \rho(r) \phi'(r) = - \int_{\phi_0}^0 dE f(E) g_3(E),$$

verifying the well-known virial theorem $\mathcal{U} = -2\mathcal{K}$, so that the total energy is

$$\mathcal{E} = \mathcal{K} + \mathcal{U} = \frac{1}{2}\mathcal{U} = -\mathcal{K}.$$

The total energy is connected to the average one-particle energy, since

$$\begin{aligned} M\bar{E} &= \int_{\phi(0)}^0 dE E n(E) = \int d^3r \int d^3v [\frac{1}{2}v^2 + \phi(r)] f(\frac{1}{2}v^2 + \phi(r)) \\ &= \mathcal{K} + 4\pi \int_0^{r_0} dr r^2 \rho(r) \phi(r) = \mathcal{K} + 2\mathcal{U} + \frac{GM^2}{r_0}. \end{aligned}$$

Hence

$$\mathcal{E} = \frac{1}{3}M\left(\bar{E} - \frac{GM}{r_0}\right). \quad (2.25)$$

In our dimensionless setup we have

$$\sigma^2(r_*x) = |\phi_0| \tilde{\sigma}^2(u(x)), \quad \tilde{\sigma}^2(u) = \frac{1}{\nu(u)} \int_u^1 ds F(s) (s - u)^{3/2} \quad (2.26)$$

and

$$\mathcal{E} = \frac{1}{2}M\phi_0 \eta,$$

where

$$\eta = \int_0^1 du x^3(u) \nu(u) = 2 \int_0^1 du x'(u) x^2(u) \nu(u) \tilde{\sigma}^2(u) \quad (2.27)$$

is the dimensionless average of the squared velocity dispersion and plays the role of a dimensionless temperature.

Eq. (2.25) now takes the form

$$\eta = \frac{2}{3}m \left(1 - \bar{s} + \frac{m}{x(1)}\right), \quad (2.28)$$

where

$$\bar{s} = 1 - \frac{\bar{E}}{\phi_0} = \frac{1}{m} \int_0^1 ds s N(s) \quad (2.29)$$

is given by the explicit expression eq. (2.16) in the DARKexp model. On the other hand, both m and $x(1)$ are not known as functions of b before a solution of eq. (2.21) is found.

3 Analytic results

As a matter of fact, we do not know how to analytically find the general solution of the DARKexp problem, as defined by eqs. (2.14) and (2.21). Some analytical results were obtained in [47] concerning the next-to-leading asymptotics near $s = 0$ of $F(s)$, $\nu(s)$, $G(s)$, and $x(s)$. In the present formulation, upon introducing functions $\xi_\nu(s)$ and $\xi_x(s)$ by

$$\nu(s) = 3\xi_\nu(s), \quad x(s) = (2s)^{1/2}(1 - hs)^{-1}\xi_x(s), \quad (3.1)$$

these results read

$$\begin{aligned} \xi_F(s) &\simeq 1 - \frac{32}{45}Ks^{1/2} - \frac{2}{45}K^2s \log s + O(s), \\ \xi_\nu(s) &\simeq 1 - \frac{1}{3}\pi Ks^{1/2} - \frac{16}{135}K^2s \log s + O(s), \\ \xi_x(s) &\simeq 1 + \frac{1}{12}\pi Ks^{1/2} + \frac{4}{225}K^2s \log s + O(s), \\ \xi_G(s) &\simeq 1 + \frac{32}{45}Ks^{1/2} + \frac{2}{45}K^2s \log s + O(s). \end{aligned} \quad (3.2)$$

Moreover, in [47] it was also argued that the next-to-leading asymptotics (3.2) is just the beginning of a complete, possibly asymptotic expansion of the form

$$\xi(s) = 1 + \sum_{n=0}^{\infty} \sum_{k=0}^n (a_{nk} + b_{nk}s^{1/2})s^n \log^{n-k} s, \quad (3.3)$$

where $a_{00} = 0$ by construction. The other coefficients are unknown, except for b_{00} and a_{10} which are given by eq. (3.2) in terms of the global normalization parameter K . We will make use of eq. (3.3) in section 5.4 to check the agreement of our numerical results with eq. (3.2).

Another (partial) analytic result is possible in the limit $b \rightarrow +\infty$, when by eq. (2.16) $\bar{s} \rightarrow 1$ and the average one-particle energy $\bar{E} \rightarrow 0$. If the mass density stays regular in this limit, thus keeping the total mass finite, then $N(s)$ must concentrate at $s = 1$ [that is $n(E)$ at $E = 0$] while $G(s)$ remains regular. Hence it is $F(s)$ that concentrates at $s = 1$ leading, by eq. (2.7) and the requirement that $\xi_\nu(0) = 1$, to the explicit analytic result

$$\lim_{b \rightarrow +\infty} \xi_\nu(u) = (1 - u)^{1/2}, \quad (3.4)$$

which is compatible with the asymptotics (3.2) because the normalization constant K [see eq. (2.22)] vanishes in the limit. In dimension-full variables we have

$$\lim_{b \rightarrow +\infty} \rho(r) = \rho_0[\phi(r)/\phi_0]^{1/2},$$

so that Poisson's eq. (2.2) becomes the Lane–Emden equation with $n = 1/2$, which does not have a known analytic solution and describes a finite-size system [3]. But it is easy to solve it numerically, for instance in our preferred form (2.3) [more precisely in the form (4.7) introduced in section 4.1]. The corresponding values of some relevant quantities, such as the dimensionless mass m and size $x(1)$, are listed in the lowest row of Table 1. Notice that in the limit $b \rightarrow +\infty$, eq. (2.15) only constrains the end value at $s = 1$ of $G(s)$, namely $G(1) = 3m$. This can be alternatively computed directly from $x(u)$ through Gauss's law $mx'(1) = x^2(1)$. The agreement of these two determinations of m provides a measure of the accuracy of our numerical solution of the DARKexp problem and will be systematically checked for many finite values of b in section 5.

4 Numerical approach

More insight on the DARKexp problem appears to be possible only through some numerical approach, which we describe in this section. In ref. [45], within a different setup and for the distinct case of $1/r$ -cusped density profiles, rather curious numerical results were reported, but without details on the specific method employed.

We first observe that eqs. (3.2) suggest a change of variable from s to $z = s^{1/2}$, so that $\xi(z^2)$, for $\xi = \xi_F, \xi_\nu, \xi_x, \xi_G$, becomes differentiable in $z = 0$. As a matter of fact, one can consider also higher powers of z in the reparametrization, such as $s = z^p$ with $p > 2$, making $\xi(z^p)$ differentiable even further in $z = 0$. In our actual computer programs we chose $p = 4$, namely $s = z^4$.

Smoothness near $s = 0$ plays an important role for numerical accuracy. For instance, even if the $s^{-1/2}$ singularity, which appears in the integrand of eq. (2.7) when $u = 0$, is integrable, it is the right neighborhood of $s = 0$ that gives the most important contribution to $\nu(u)$ when $u \gtrsim 0$ and the reparametrization $s = z^p$ improves accuracy in the integration. Furthermore, by tuning the value of the free parameter h , we can make each $\xi(z^p)$ to have a variation of order one on the interval $[0, 1]$, besides being certainly smooth there. It follows that $\xi(z^p)$ can be approximated very accurately and effectively by an expansion in a relatively small number of scaled and shifted Chebyshev polynomials $T_n(2z - 1)$.

Hence our numerical approach starts by discretizing the interval $[0, 1]$ using $N+1$ Chebyshev points of the second kind, according to

$$s_k = z_k^p, \quad z_k = 2 \sin^2\left(\frac{k\pi}{2N}\right), \quad k = 0, 1, \dots, N, \quad (4.1)$$

so that the function $\xi(s)$ is replaced by the discrete array $\{\xi(s_k), k = 0, 1, \dots, N\}$. At the same time, this array uniquely defines, for all $s \in [0, 1]$, a polynomial approximation to the exact $\xi(s)$ as

$$\xi(z^p) \approx \sum_{n=0}^N c_n T_n(2z - 1), \quad (4.2)$$

which allows an accurate calculation of the integral transforms in eqs. (2.7) and (2.12). These transforms read for the ξ functions

$$\xi_\nu(u) = \frac{1}{3}K \int_u^1 ds s^{-1} (s-u)^{1/2} (1-hs)^{5/2} \xi_F(s). \quad (4.3)$$

and

$$\xi_G(s) = \frac{8}{3\pi s^2} (1-hs)^{5/2} \int_0^s du (s-u)^{-1/2} \left[\frac{u^{1/2} \xi_x(u)}{1-hu} \right]^3, \quad (4.4)$$

The map from the function values $\xi(s_k)$ [or local functions of them as in the r.h.s. of eq. (4.4)] to the Chebyshev coefficients c_n can be performed very efficiently through Clenshaw–Curtis formulas (*a.k.a.* fast discrete cosine transform).

Let us also observe that, by construction, $\xi(0) = 1$ for all four ξ_F, ξ_ν, ξ_x and ξ_G , so that there are only N independent unknowns, that we choose to be those of the array $\{\xi_F(s_k), k = 1, \dots, N\}$.

Quite obviously, the accuracy of the numerical approach described in the rest of this section depends on N , that is on the size of the discretization grid over the interval of interest

[0, 1]. Since the execution speed on any computer rapidly increases for increasing N , some trade off is required. Thanks to the excellent properties of Chebyshev interpolation, it turns out that a very good accuracy can be attained, for a whole range of b values, already with $N = 400$, while keeping the required computational resources well within those of a powerful workstation. We have estimated this accuracy to be better than 10^{-9} for all grid values, by comparison with the results obtained when $N = 10^3$ and by other means described in the Appendix.

4.1 Integral transforms and Poisson's equation

The calculation of the integral transforms in eqs. (4.3) and (4.4) is made fast, fully preserving accuracy, by pre-computing the relevant integrals with the Chebyshev polynomials $T_n(2z-1)$. For instance, for eq. (4.3) we have

$$\xi_\nu(z^p) \approx K \sum_{n=0}^N c_{F,n} I_n^{(F\nu)}(z),$$

where

$$I_n^{(F\nu)}(z) = \frac{1}{3p} \int_z^1 dy y^{-1} (y^p - z^p)^{1/2} (1 - hz^p)^{5/2} T_n(2y - 1). \quad (4.5)$$

Hence we may set

$$\xi_\nu(s_k) \approx \sum_{n=0}^N c_{\nu,n} T_n(2z_k - 1) = K \sum_{n=0}^N c_{F,n} I_{nk}^{(F\nu)}, \quad I_{nk}^{(F\nu)} \equiv I_n^{(F\nu)}(z_k), \quad (4.6)$$

from which, if necessary, the $c_{\nu,n}$ can be recovered by the fast Clenshaw–Curtis algorithm. The important point is that only a vector–matrix multiplication is needed in this $\xi_F \rightarrow \xi_\nu$ step, since the matrix entries $I_{nk}^{(F\nu)}$ can be computed, for a given choice of N , once and for all. It should also be noticed that the constant K is fixed by the requirement that $\xi_\nu(0) = 1$, that is

$$K^{-1} = \frac{1}{3} \int_0^1 ds \frac{(1 - hs)^{5/2}}{s^{1/2}} \xi_F(s) \approx \sum_{n=0}^N c_{F,n} I_{n0}^{(F\nu)}.$$

The second step $\nu \rightarrow x$ in the chain (2.14) requires to numerically solve Poisson's equation, in either one of the two forms in eq. (2.2) or eq. (2.3). In our setup the latter form is more appropriate, since the grid is fixed in the u variable. Using the form of eq. (2.2) where x is the independent variable has drawbacks for accuracy and/or speed, especially if $x(1)$ happens to be very large. On the other hand, in the form of eq. (2.3) where u is the independent variable, high accuracy is possible also when $x(1)$ becomes very large, but special care is needed for the initial conditions $x \simeq (2u)^{1/2}$ as $u \rightarrow 0$. We found it convenient to reformulate eq. (2.3) as follows

$$\xi_x(e^y) = (1 - h e^y) e^{\gamma(y)/2}, \quad \gamma'' = \frac{3}{2} + 2\gamma' + \frac{1}{2}\gamma'^2 - \frac{3}{2}\xi_\nu(1 + \gamma')^3 e^\gamma. \quad (4.7)$$

The initial conditions on γ now read $\lim_{y \rightarrow -\infty} (\gamma, \gamma') = (0, 0)$ and can be implemented numerically by setting $(\gamma, \gamma') = (0, 0)$ at any large negative value y_0 such that e^{y_0} vanishes as double-precision floating number. Notice also that values of $\xi_\nu(u)$ at generic values of u are needed to solve eq. (4.7) and the most effective interpolation is just the Chebyshev one.

The final outcome is the array $\{\xi_x(s_k), k = 0, 1, \dots, N\}$, which is used in the last step $x \rightarrow G$ with the same reduction of the integral transform (4.4) to a matrix–vector multiplication as in the first step. The only caveat, from the numerical point of view, is to avoid the multiplication of the possibly very large/small prefactor $s^{-2}(1+rs)^{5/2}$ by the possibly very small/large integral when $s \rightarrow 0$ or both s and h are close to 1. This is accomplished by the following change of integration variable

$$u = u(t, s, h) = s(1-t^2) \frac{1+h(1-s)}{1+h(1-s-t^2)},$$

which transforms eq. (4.4) into the smoother expression

$$\xi_G(s) = \frac{8}{3\pi} [1+h(1-s)]^{5/2} \int_0^1 dt \left[\frac{(1-t^2)^{1/2}}{1+h(1-t^2)(1-s)} \xi_x(u(t, s, h)) \right]^3. \quad (4.8)$$

Then we can write

$$[\xi_x(z^p)]^3 \approx \sum_{n=0}^N c_{x,n} T_n(2z-1), \quad \xi_G(s_k) \approx \sum_{n=0}^N c_{x,n} I_{nk}^{(xG)},$$

where the pre-computable matrix entries read

$$I_{nk}^{(xG)} = \frac{8}{3\pi} [1+h(1-s_k)]^{5/2} \int_0^1 dt \left[\frac{(1-t^2)^{1/2}}{1+h(1-t^2)(1-s_k)} T_n(2[u(t, s_k, h)]^{1/4} - 1) \right]^3. \quad (4.9)$$

As discussed in the Appendix, the accuracy of this approach crucially depends on the convergence toward zero of the coefficients $c_{x,n}$ as n grows. In turns, this depends on the behavior of $\xi_x(s)$ as $s \rightarrow 1$. The behavior as $s \rightarrow 0$ is not as important, in spite of the logarithmic singularity in eq. (3.2), because of the extra powers of u appearing in the integrand of eq. (4.4). We see that the free parameter h can be fixed beforehand to guarantee that $\xi_x(1)$ does not becomes too large, thus preventing the risk of a poor convergence of the coefficients $c_{x,n}$.

A worthwhile byproduct of the smoother rewriting (4.8) of the map from ξ_x to ξ_G is the rigorous derivation of the large–distance behavior, stated without details in section 2.1, of the mass density in a system with infinite size. In such a system, which by assumption has a finite total mass M , the gravitational potential $\phi(r)$ dies off at radial infinity as $M(4\pi r)^{-1}$ (recall that $4\pi G = 1$). In the dimensionless setup this reads $x(u) \simeq m(1-u)^{-1}$ as $u \rightarrow 1$. Then, setting $h = 1$, from eq. (3.1) we see that $\xi_x(1) = 2^{-1/2}m$ is finite and that a cubic pole as $u \rightarrow 1$ appears in the integrand of eq. (4.4) when $s \rightarrow 1$. The smoother rewriting (4.8) explicitly shows that this exactly compensate the the zero coming from the prefactor $(1-s)^{5/2}$ in eq. (4.4) when $h = 1$. Hence $\xi_G(1)$ is finite and by the fundamental equation (2.21) we see that $\xi_F(1)$ must be finite and larger than zero. Then a simple power counting in eq. (4.3) shows that $\xi_\nu(u) \sim (1-u)^4$ as $u \rightarrow 1$ or, equivalently, $\rho(r) \sim r^{-4}$ as $r \rightarrow \infty$.

Altogether, the method just described turns out to be fast and accurate in computing the numbers $\{\xi_G(s_k), k = 0, 1, \dots, N\}$ from given numbers $\{\xi_F(s_k), k = 0, 1, \dots, N\}$, that is recovering the approximated $\xi_G(s)$ from a given approximated $\xi_F(s)$. In principle, one could consider also the reverse computation along the chain eq. (2.14), that is from $\xi_G(s)$ to $\xi_F(s)$, with the apparent advantage of reducing eq. (2.3) to an explicit calculation of ν from x . There are two shortcomings of this reverse approach: differentiation introduces larger numerical errors than integration and, most importantly, there is no guarantee of preserving positivity when going from an arbitrary positive $\xi_G(s)$ back to $\xi_F(s)$.

4.2 System of non-linear equations

With ξ_G accurately computable from ξ_F , eq. (2.21) becomes, in our discretized setup, a system of N non-linear equations for the N unknowns $\xi_F(s_k)$. We need to numerically solve these equations, which means to make the (relative) residuals

$$R_k[\xi_F] = \frac{\xi_F(s_k)\xi_G(s_k)}{A(b s_k)} - 1, \quad k = 1, 2, \dots, N, \quad (4.10)$$

as small as possible. On general grounds, due to numerical roundoffs, the magnitudes $|R_k|$ cannot be smaller than the machine epsilon, namely $2.22044\dots \cdot 10^{-16}$ in double-precision. But any algorithm that tries to minimize the $|R_k|$, assuming that there exist an exact, analytic solution, will stop at values that can be much larger than that, depending on N , on the N -dimensional numerical neighborhood of the solution, on the algorithm itself and on how sensible it is on the accuracy in the calculation of the chain eq. (2.14). The problem is to determine when small is small enough, since we should expect that, by varying b , certain exact solutions of eq. (2.21) might appear, disappear, coalesce or more simply become more difficult to pinpoint with numbers. In principle, one would like to disentangle, if necessary, the case when the numerical ξ_F is a poor approximation of an exact solution from the case when there no exact solution at all. This is a difficult task and, in the absence of analytic results concerning the existence of solutions for any given value of b , it is a numerical task beyond the scope of this work. Here we want to present a class of convincing numerical solutions, rather than rule out the existence of solutions for certain values of b . In other words, we will not state that there exist no solution when b takes values for which we cannot not produce accurate numerical solutions.

An accurate numerical solution, as we define it, is any output of a program devised to minimize the residuals that succeeds to the point that

$$\mathcal{R} \equiv \max_k |R_k| < \epsilon, \quad \epsilon \equiv 10^{-11}. \quad (4.11)$$

The specific value of ϵ was empirically determined as the typical one worth attaining and attainable upon optimization of all steps of the calculation. In other words, we found that $\epsilon = 10^{-11}$ is close enough to the limit of the double-precision accuracy for the problem at hand. More details on this result can be found in the next section and in the Appendix. However, while very often we obtained residuals much smaller than eq. (4.11), with \mathcal{R} even of order 10^{-14} , we regard as acceptable solutions also those obtained in a special class of cases in which the bound (4.11) is not satisfied, although the residuals are as small as 10^{-8} . The reason for this exception to eq. (4.11) is that we can identify quite precisely the source of extra numerical errors causing the degraded accuracy and that these *reasonably inaccurate* numerical solutions fit very well into a continuous b -dependent family.

Let us now describe the two numerical approaches we use to deal with eq. (2.21).

The first, straightforward approach is to start from some initial $\xi_F^{(0)}$ and then iterate as follows

$$\xi_F^{(n+1)}(s_k) = (1 - \alpha)\xi_F^{(n)}(s_k) + \alpha \frac{A_b(s_k)}{\xi_G^{(n)}(s_k)}, \quad k = 1, 2, \dots, N, \quad (4.12)$$

with α a damping parameter that might help convergence to some fixed point, which would then be a solution of our problem. Of course, this method can work only if there are stable

fixed points, that is such that the Jacobian matrix

$$J_{kn}(\alpha) = (1 - \alpha)\delta_{kn} + \alpha A_b(s_k) \frac{\partial[\xi_G(s_k)]^{-1}}{\partial \xi_F(s_n)}, \quad (4.13)$$

when evaluated at such fixed point, has eigenvalues with magnitudes all less than one for some value of α . Even so, the iteration will converge only if the initial $\xi_F^{(0)}$ is in the basin of attraction of some stable fixed point. Moreover, due to numerical roundoffs, there cannot be true convergence to a fixed point. Rather, the sequence $\xi_F^{(n)}$ will indefinitely and more or less randomly and tightly fluctuate around the stable fixed point profile, provided the residuals are small enough. It will become apparent in the next section that residuals satisfying eq. (4.11) are indeed small enough.

The simple iteration method should be tried first. If it fails we can resort to the second approach, possibly much slower but safer and much richer of tunable parameters, that is some general-purpose algorithm for systems of non-linear equations (see *e.g.* [49]). For instance one that, starting from an initial $\xi_F^{(0)}$, iteratively minimizes some positive-definite scalar expression that vanishes at the solution, such as

$$\mathcal{F}[\xi_F] = \sum_{k=0}^N w_k (R_k[\xi_F])^2, \quad w_k > 0, \quad (4.14)$$

or any other scalar, positive-definite expression that vanishes when $R_k = 0$. This quantity is usually called the *objective function*.

The obvious problem of any such algorithm is that it can only find local minima of the objective function, which could in principle be different for different starting points. The actual solutions of eq. (2.21) for any given b correspond to global minima where the residuals vanish in the numerical sense, namely that, according to our understanding, satisfy the criterion (4.11).

The two approaches just described can be compared, when both are successful, to verify their consistency if the starting $\xi_F^{(0)}$ is the same, since they have a different structure of basins of attraction. They can also be mixed, to improve the overall speed and/or accuracy of the calculation and to try and disentangle global minima from local minima of the objective function.

Finally, let us consider the choice of the array $\xi_F^{(0)}$ on which to start the minimization run. A convenient strategy is to find, by trial and error for at least one value $b = b_0$, an acceptable solution. Next, this ξ_F can be used as initial configuration for another run with a new value $b = b_1$, close enough to b_0 , relying on the continuity in b of the solution. Then this process can be repeated as many times as possible, perhaps adjusting each time the increment of b and/or using initial configurations obtained by extrapolation in b . For the first run at $b = b_0$ one could start for instance from the simplest initial array $\xi_F^{(0)} = 1$, but any other choice is possible, as long as it does lead to an acceptable solution. The results reported in section 5 have been obtained using this strategy with $b_0 = 2$ and $\xi_F^{(0)} = 1$.

5 Numerical results

We begin by describing in detail, when $b = 2$, the computation of a profile ξ_F satisfying eq. (2.21), in the sense of criterion (4.11), using both methods described in the previous

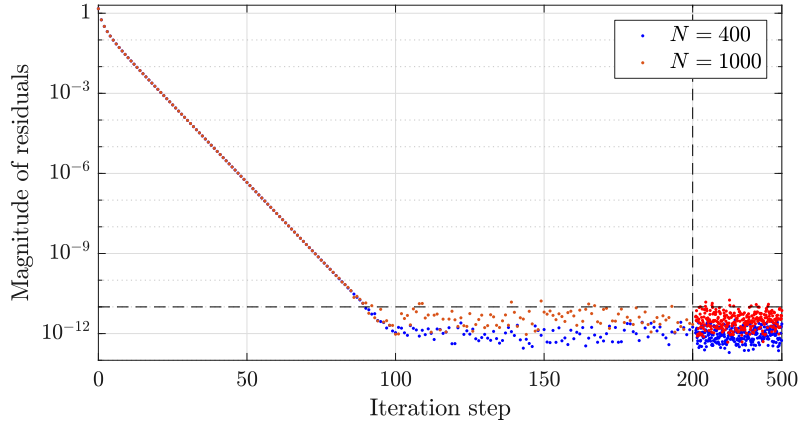


Figure 1. The value of \mathcal{R} [see eqs. (4.10) and (4.11)] at each iteration of the map (4.12). Almost all values in the fluctuating plateau satisfy the criterion (4.11).

Iteration	Func-count	Residual	First-Order optimality	Lambda	Norm of step
0	1	153.829	3.66	0.01	
1	2	12.5131	0.663	0.001	11.0553
2	3	0.625631	0.121	0.0001	7.61673
3	4	0.00603712	0.0119	1e-05	2.92556
4	5	1.3804e-06	0.000209	1e-06	0.334842
5	6	3.97629e-11	1.16e-06	1e-07	0.00395832
6	7	1.10488e-16	2.13e-09	1e-08	1.81568e-05
7	8	1.40243e-22	2.41e-12	1e-09	1.01033e-08
8	9	6.65201e-23	1.5e-12	1e-10	1.42617e-11
9	13	4.30925e-23	9.91e-13	1e-07	2.9711e-11
10	19	2.05362e-23	5.42e-13	0.01	2.28227e-11

`fsolve` stopped because the relative [norm of the current step](#), 1.618881e-16, is less than [options.StepTolerance](#) = 1.000000e-15. The sum of squared function values, $r = 2.053619e-23$, is less than [sqrt\(options.FunctionTolerance\)](#) = 1.000000e-10.

Figure 2. Output of MATLAB `fsolve` running the Levenberg–Marquardt algorithm when $b = 2$ and $N = 400$. The 'Residual' column exhibits the values of the objective function $\mathcal{F}[\xi_F]$ in eq. (4.14) with unit weights w_k . Notice the little irrelevant MATLAB bug in the output, namely the final 'Residual' compared to the square root of *FunctionTolerance* rather than *FunctionTolerance* itself.

section. The initial profile is $\xi_F^{(0)}(s) = 1$ and the free parameter h is momentarily set to 0. In this case the iterative map (4.12) converges rather rapidly already with $\alpha = 1$. Just as successful, albeit slower, is the minimization of the objective function $\mathcal{F}[\xi_F]$ in eq. (4.14) with the weights $w_k \equiv 1$.

First method

Using $N = 400$ Chebyshev points, after less than 100 iterations of the map (4.12), the monotonic decreasing trend of the residuals R_k [see eq. (4.10)] has come to an end. Then the R_k keep fluctuating with values of order 10^{-12} [see Fig. 1]. We can take as solution any profile ξ_F satisfying eq. (4.11). No accuracy gain is obtained using 10^3 Chebyshev points [see Fig. 1]. On the contrary, as should be expected if the calculation is close to its double-precision limit, the fluctuating residuals with $N = 10^3$ are slightly larger than those with $N = 400$, because of the increased number of roundoffs.

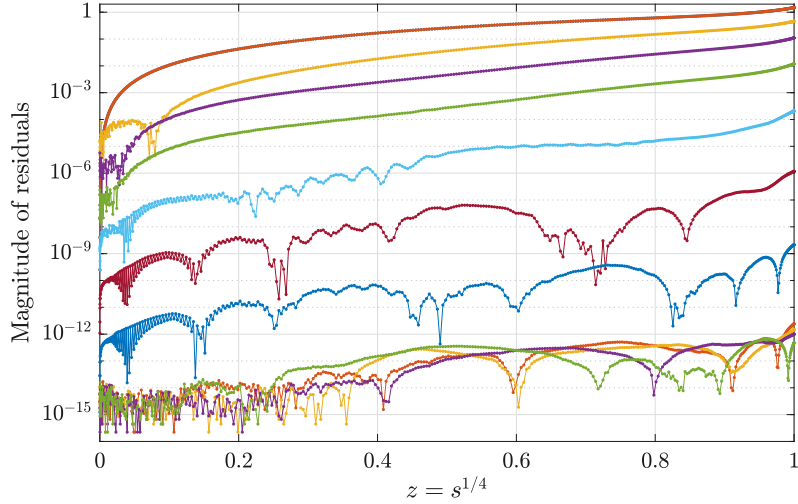


Figure 3. The absolute values of the residuals R_k [see eq. (4.10)] at each iteration of `fsolve` running as in Fig 2. This is a successful run according to the criterion (4.11). Notice the appearance of rugged fluctuations which are typical of numerical roundoffs.

Second method

The minimization algorithm we adopted is `fsolve` in MATLAB R2017b. We first run it with $N = 400$ points, until it stops because the proposed change in ξ_F is too small [see Fig. 2 and 3]. This is a successful run, since the final residuals satisfy the condition (4.11). We again repeat the calculation with 10^3 , with no increase of accuracy on the residuals.

In terms of the Chebyshev interpolating polynomials, we find that

$$\max_s |\xi_F^{(N=400)}(s) - \xi_F^{(N=1000)}(s)| \sim 10^{-11} ,$$

for both methods. The excellent agreement between the two calculations, with $N = 400$ and $N = 10^3$, can be traced back to the fast decay of the Chebyshev coefficients of $\xi_F(z^4)$ and $\xi_x^3(z^4)$, which are plotted in Fig. 4. Denoting with $\xi_F^{(A)}$ and $\xi_F^{(B)}$ the profiles obtained by the two methods, we find that

$$\max_k |\xi_F^{(A)}(s_k) - \xi_F^{(B)}(s_k)| \sim 10^{-11} ,$$

both for $N = 400$ and $N = 1000$. Another check on the stability of the calculation is possible by varying the free parameter h . We verify that $(1 + hs)^{5/2}\xi_F(s, h)$ indeed does not depend on h , within order 10^{-13} , as long as h is not too close to 1. When h gets too close to 1, $\xi_F(1, h)$ becomes very large, compromising the accuracy of the Chebyshev approximation. Altogether, according to the analysis of the Appendix, we expect our numerical ξ_F to differ at most by order 10^{-10} from the exact solution.

The initial and final profiles of ξ_F , ξ_ν , ξ_x and ξ_G , as functions of s are plotted in Fig. 5.

5.1 Solutions of the first kind

To compute solutions for other values of b we follow the strategy outlined at the end of the previous section. We use the final ξ_F with $b = 2$ as input for a new run with, say, $b = 2.1$,

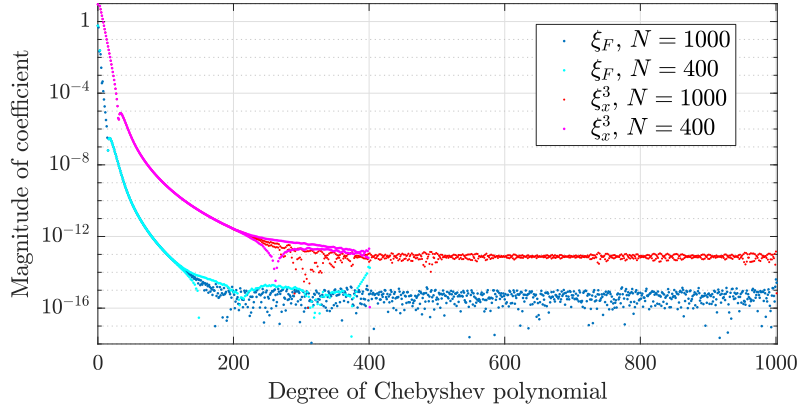


Figure 4. The Chebyshev coefficients of $\xi_F(z^4)$ and $\xi_x^3(z^4)$ when $b = 2$.

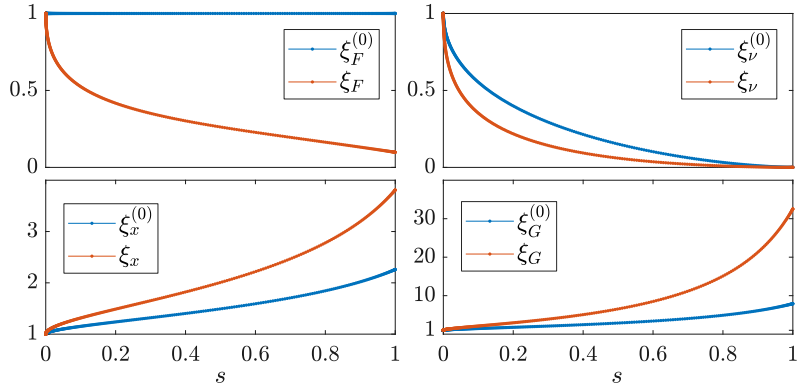


Figure 5. Initial and final profiles when $b = 2$.

using either one of the two methods. If this run is successful, we have a solution at the new value $b = 2.1$. If not, we reduce the increment of b until a successful run is realized. It turns out that increasing b from the initial value $b = 2$ is quite easy and the incremental step can be much larger than 0.1. Even more, we find that one can always start from the initial profile $\xi_F^{(0)}(s) = 1$ with only a little extra cost in computer time. This is due to the behavior of ξ_F , ξ_ν , ξ_x and ξ_G as functions of b , as evident from Fig 6. The size $x(1)$ shrinks with increasing b , further improving accuracy and convergence rate to the solution.

In Table 1 we list the number of iterations N_{iter} , the value of the residual R and the values of the of K , $x(1)$, m and the dimensionless temperature η [see eq. (2.27)] for some selected values in the interval $2 \leq b \leq 100$. Notice that m can be obtained in two, numerically inequivalent ways:

m_1 : in terms of K and b as in eq. (2.22), with an accuracy that depends on how small are the residuals and how are they arranged around 0;

m_2 : in terms of $x(1)$ and $x'(1)$, relying on Gauss's law, $mx'(1) = x^2(1)$, with an accuracy directly related to that of the solution of Poisson's equation.

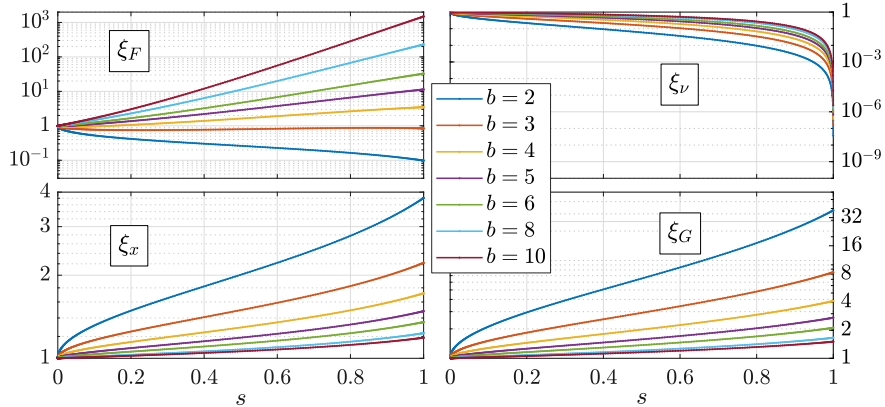


Figure 6. The four profiles ξ_F , ξ_ν , ξ_x and ξ_G at selected values of $b \geq 2$, with $h = 0$ [see eqs. (2.19), (2.20) and (3.1)]. These are profiles corresponding to solutions of the first kind.

b	N_{iter}	\mathcal{R}	K	$x(1)$	m	η	Δm	$\Delta \eta$
2	91	$6.60 \cdot 10^{-13}$	3.47182	5.38834	2.11565	0.93765	$6.18 \cdot 10^{-12}$	$3.39 \cdot 10^{-12}$
3	34	$3.86 \cdot 10^{-13}$	1.83567	3.13586	1.82206	0.99742	$4.08 \cdot 10^{-12}$	$3.10 \cdot 10^{-12}$
4	25	$3.10 \cdot 10^{-13}$	1.01445	2.43178	1.74643	1.08028	$1.28 \cdot 10^{-12}$	$3.52 \cdot 10^{-12}$
5	19	$5.76 \cdot 10^{-14}$	0.54827	2.09556	1.73452	1.16810	$1.65 \cdot 10^{-13}$	$3.82 \cdot 10^{-12}$
7	13	$2.93 \cdot 10^{-14}$	0.14406	1.80740	1.77751	1.33088	$1.16 \cdot 10^{-12}$	$4.76 \cdot 10^{-12}$
10	9	$4.49 \cdot 10^{-14}$	0.01528	1.67974	1.86851	1.50996	$8.17 \cdot 10^{-13}$	$6.81 \cdot 10^{-12}$
20	6	$4.95 \cdot 10^{-14}$	$3.00 \cdot 10^{-6}$	1.61608	2.02344	1.75643	$6.50 \cdot 10^{-12}$	$1.39 \cdot 10^{-11}$
100	4	$2.52 \cdot 10^{-14}$	$1.44 \cdot 10^{-39}$	1.59316	2.15456	1.95689	$5.39 \cdot 10^{-11}$	$7.29 \cdot 10^{-11}$
∞	n.a.	n.a.	0	1.58927	2.18738	2.00705	$1.26 \cdot 10^{-10}$	$1.62 \cdot 10^{-7}$

Table 1. Values of relevant parameters for $b \geq 2$. For brevity we give only five decimal figures for the quantities of order 1, but we estimate our accuracy to be twice as much, except perhaps for $b = \infty$. N_{iter} is the number of iterations needed by the simple map (4.12) to satisfy the bound (4.11). After that, the minimization algorithm is run and \mathcal{R} is the residual value when it stops.

A similar observation applies to η :

η_1 : in terms of m_1 , \bar{s} and $x(1)$, as in eq. (2.28);

η_2 : from the integral in eq. (2.27), that is $\eta = 12 \cdot 2^{3/2} \int_0^1 dz z^9 \xi_x^3(z^4) \xi_\nu(z^4)$, computed through Chebyshev quadrature.

The values listed in Table 1 are the mean values $m = \frac{1}{2}(m_1 + m_2)$ and $\eta = \frac{1}{2}(\eta_1 + \eta_2)$, while $\Delta m = |m_1 - m_2|$ and $\Delta \eta = |\eta_1 - \eta_2|$. The agreement between the two determinations of m and η is better than our accuracy estimate, except when $b = \infty$. The slightly worse accuracy in this case can be traced back to the square-root behavior of $\xi_\nu(u)$ near $u = 1$ [see eq. (3.4)], which makes Chebyshev quadratures less efficient, especially concerning the calculation of η_2 .

In the opposite direction, that is when b is decreased, we find that K , $x(1)$, m and η monotonically increase. At the same time, the number of iterations of the map eq. (4.12) required to reach an accurate solution increases much more rapidly. A significant time saving is then obtained by starting each new run from the final configuration obtained in the preceding

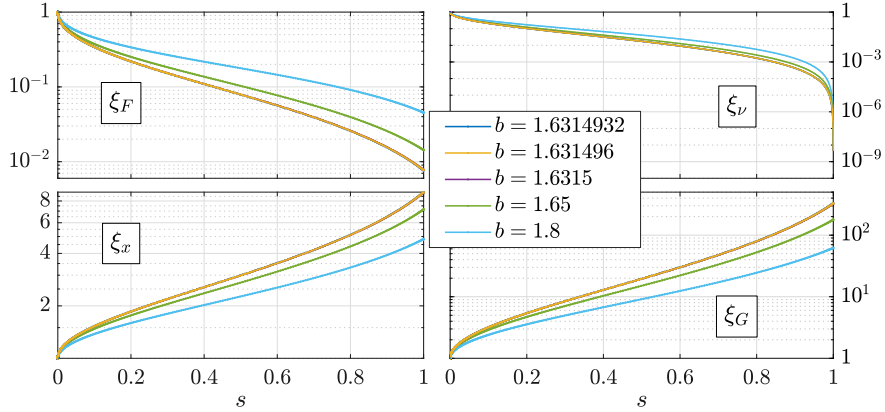


Figure 7. First kind ξ_F , ξ_ν , ξ_x and ξ_G at selected values of $b < 2$, with $h = 0$ [see eqs. (2.19), (2.20) and (3.1)]. The profiles corresponding to the first three values of b are indistinguishable on the scale of the plot.

b	N_{iter}	\mathcal{R}	K	$x(1)$	m	η	Δm
1.6314932	644496	$4.06 \cdot 10^{-12}$	5.45442	12.71729	2.82232	0.95194	$1.14 \cdot 10^{-11}$
1.6314937	180107	$5.70 \cdot 10^{-12}$	5.45239	12.70294	2.82127	0.95190	$5.23 \cdot 10^{-12}$
1.631496	84342	$7.08 \cdot 10^{-12}$	5.44927	12.68105	2.81966	0.95184	$1.33 \cdot 10^{-11}$
1.63150	21589	$2.09 \cdot 10^{-12}$	5.44625	12.65990	2.81810	0.95178	$2.68 \cdot 10^{-11}$
1.63155	6385	$6.83 \cdot 10^{-12}$	5.43031	12.54914	2.80991	0.95147	$9.12 \cdot 10^{-12}$
1.65	456	$5.30 \cdot 10^{-13}$	5.01071	10.11928	2.61357	0.94383	$1.25 \cdot 10^{-11}$
1.8	150	$5.49 \cdot 10^{-13}$	4.10702	6.84120	2.28767	0.93489	$9.53 \cdot 10^{-12}$

Table 2. Values of relevant parameters for $b < 2$. N_{iter} is the cumulative number of iterations needed to satisfy the bound (4.11). For lack of space we do not list the values of $\Delta\eta$, which anyway are of the same order of Δm .

run, adapting the step down in b to guarantee a reasonably fast convergence. Some of the profiles are plotted in Fig 7, while the global data shown in Table 1 for $b \geq 2$ are now listed in Table 2 for few selected values of b . One notices the steep rise of K , $x(1)$, m and η as b approaches the smallest value in the table, $b = 1.6314932$. Repeating some of the runs with $N = 1000$ Chebyshev points just confirm the $N = 400$ results.

Clearly the solutions just listed for $b \geq 2$ and for $1.6314932 \leq b < 2$ belong to a continuous family, which we call of the first kind, with the prominent feature that

$$\xi_F(s, b) < \xi_F(s, b'), \quad \forall s \in [0, 1], \quad \text{if } b < b'. \quad (5.1)$$

As a consequence, ξ_ν also increases with b while ξ_x and ξ_G uniformly decrease [this is due to the positivity property highlighted below eq. (2.4)]. Thus K and $x(1)$ are both monotonically decreasing with b . The behavior of the m and η in the interval $1.6314932 \leq b \leq 10$ is not monotonic, but we suspect η to be monotonically increasing for all $b > 2$.

At each solution found, it is of interest to compute through finite differences a good approximation of the Jacobian matrix $J(\alpha)$, eq. (4.13), associated to the iterated map (4.12). We find that all eigenvalues of $J(1)$ have magnitude smaller than 1, as expected since the

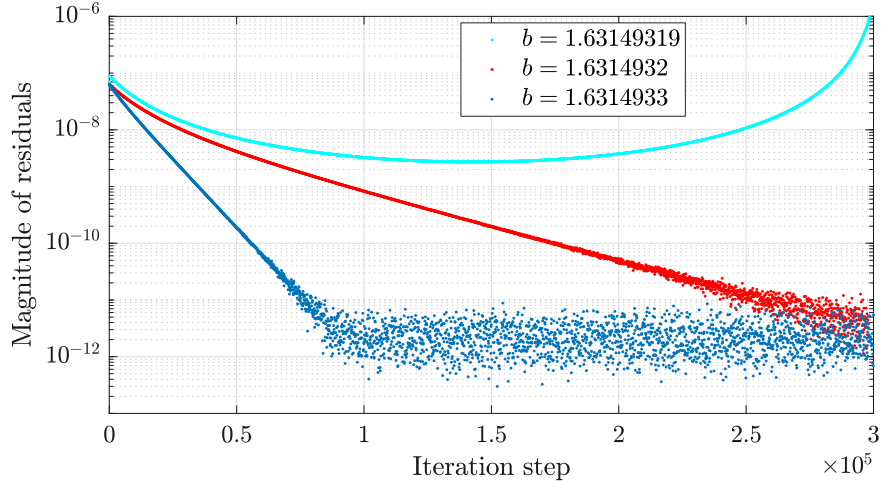


Figure 8. The evolution of \mathcal{R} , the largest residual magnitude, along the iterated map (4.12) with comparable initial conditions, for three very close values of b .

iterated map always converges. However the largest eigenvalue, which is real, approaches unity as $b \rightarrow 1.6314932$, causing the observed slow-down.

We find it impossible to go below $b = 1.6314932$ by any amounts of order 10^{-8} or more, while preserving the default smallness of the residuals, that is $\mathcal{R} < 10^{11}$. In Fig. 8 we plot the residual \mathcal{R} during three runs of the iterated map (4.12), when b takes the values $b = 1.6314933$, $b = 1.6314932$ and $b = 1.63149319$. The first run starts at the ξ_F that satisfies eq. (2.21), in the sense of criterion (4.11), when $b = 1.6314934$; the second and the third start both at the solution corresponding to $b = 1.6314933$, when we still obtain a successful run, as evident from Fig. 8. Notice that, by construction, the initial \mathcal{R} is slightly less than 10^{-7} in all three cases. While the iteration with $b = 1.6314932$ still manages to converge, albeit very slowly, the iteration with $b = 1.63149319$, after a decrease to values of \mathcal{R} of order 10^{-9} , eventually begins to diverge. Since we expect the solutions to depend continuously on b , we infer that at a certain value $b = b_1$ between 1.63149319 and $b = 1.6314932$ two solutions of eq. (2.21) that existed for $b > b_1$ have coalesced and there are no solutions at all for $b \lesssim b_1$.

Up to now, however, we have only found one solution for each value of $b > b_1$, either starting from $\xi_F^{(0)}(s) = 1$ or relying on continuity in b and using as starting point of a new run the final profile of a successful preceding run. This means that, when descending from $b = 2$, the final profile of ξ_F is uniformly smaller than the initial one [see eq. (5.1)]. In this way we might have missed the possibility of even smaller ξ_F solutions. Indeed, in the next subsection we describe such other solution family for $b > b_1$.

5.2 Solutions of the second kind

Suppose we use the final ξ_F found for $b = 1.6314932$, the value closest to the boundary value b_1 , when we still obtain an accurate solution, as starting point for a new run with a *larger* value of b , say the next value in Table 2, $b = 1.6314937$. This ξ_F is uniformly smaller than the one we have already found as accurate solution to eq. (2.21) when $b = 1.6314937$ and, correspondingly, $K(1.6314932) > K(1.6314937)$. We find that the iterated map (4.12) just reproduces that solution, while the minimization algorithm fails to reach the desired accuracy,

Iteration	Func-count	Residual	First-Order optimality	Lambda	Norm of step
0	1	0.777355	0.11	0.01	
1	2	0.155204	0.00472	0.001	0.51731
2	3	0.139343	0.00564	0.0001	2.1513
3	5	0.0997787	0.0162	0.001	3.95805
4	6	0.0542115	0.0233	0.0001	4.40095
5	8	0.0197697	0.0146	0.001	3.17656
6	9	0.00656141	0.0068	0.0001	1.9399
7	10	0.00388273	0.016	1e-05	2.57655
8	11	1.23681e-05	0.000861	1e-06	0.486604
9	12	4.14207e-09	1.65e-05	1e-07	0.0190277
10	13	3.44506e-15	1.24e-08	1e-08	8.07609e-05
11	14	1.8339e-17	1.1e-09	1e-09	9.53632e-07
12	15	1.87693e-20	2.92e-11	1e-10	5.2064e-09
13	16	3.95334e-21	8.66e-12	1e-11	1.2548e-09
14	24	3.35635e-21	1.02e-11	0.0001	8.63293e-10
15	31	2.37684e-21	5.99e-12	100	8.9113e-13

`fsolve` stopped because the relative [norm of the current step](#), 3.663829e-16, is less than `options.StepTolerance` = 1.000000e-15. The sum of squared function values, $r = 2.376841e-21$, is less than `sqrt(options.FunctionTolerance)` = 1.000000e-10.

Figure 9. Output of MATLAB `fsolve` running the Levenberg–Marquardt algorithm when $b = 1.8$ and $N = 400$, starting from the ξ_F profile obtained for $b = 1.6314932$.

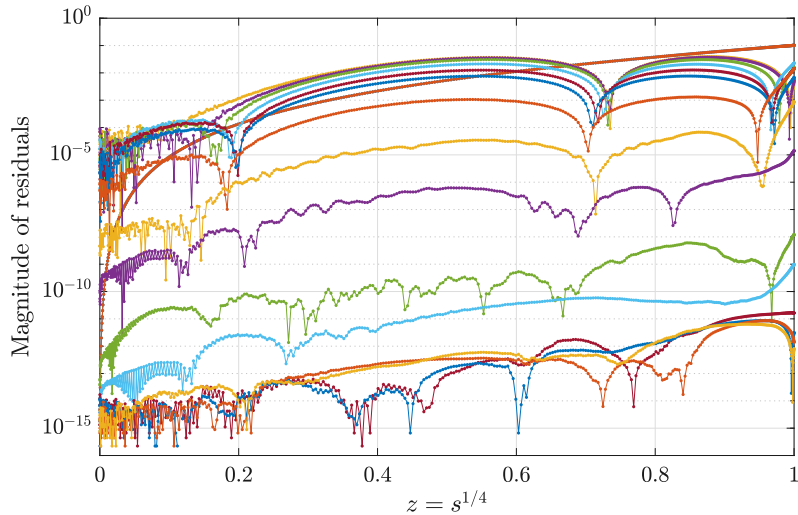


Figure 10. The absolute values of the residuals R_k at each iteration of `fsolve` running as in Fig 9.

even playing around with its many tunable parameters, in any reasonable amount of time. Within our hypothesis of the coalescence of two roots, this probably means that $b = 1.6314937$ is still too close to coalescence value b_1 , for the minimization algorithm to disentangle the new solution we are seeking for from the nearby solution we have already found.

However, since at first we only need to find the new solution for just one value of b , let us consider a larger value of b , far enough from the coalescence region. Let us pick $b = 1.8$, the largest value in table 1, as starting value for the sought second branch of solutions. We discover that both methods to solve eq. (2.21) are successful, but yield different results. While in 152 iterations the iterated map (4.12) with $\alpha = 1$ falls back to the solution with $K = 4.107017\dots$

b	\mathcal{R}	K	$x(1)$	m	η	Δm	$\Delta \eta$
1.6314937	$9.23 \cdot 10^{-12}$	5.45699	12.73540	2.82365	0.95199	$2.96 \cdot 10^{-12}$	$6.25 \cdot 10^{-13}$
1.631496	$1.47 \cdot 10^{-12}$	5.46010	12.75743	2.82526	0.95205	$2.62 \cdot 10^{-11}$	$4.67 \cdot 10^{-12}$
1.63150	$8.16 \cdot 10^{-12}$	5.46312	12.77884	2.82683	0.95211	$2.40 \cdot 10^{-11}$	$8.22 \cdot 10^{-12}$
1.63155	$7.97 \cdot 10^{-13}$	5.47903	12.89281	2.83512	0.95242	$2.51 \cdot 10^{-11}$	$6.31 \cdot 10^{-12}$
1.65	$6.39 \cdot 10^{-13}$	5.88779	16.55156	3.07105	0.96013	$3.39 \cdot 10^{-11}$	$7.05 \cdot 10^{-12}$
1.8	$6.39 \cdot 10^{-12}$	6.69267	35.11926	3.72791	0.95621	$7.29 \cdot 10^{-11}$	$6.63 \cdot 10^{-12}$

Table 3. Values of relevant parameters for $b \leq 1.8$ in the family of solutions of the second kind.

b	\mathcal{R}	K	$x(1)$	m	η	Δm	$\Delta \eta$
1.9	$3.77 \cdot 10^{-12}$	6.96731	59.91614	4.05790	0.92821	$2.38 \cdot 10^{-10}$	$9.47 \cdot 10^{-12}$
1.96	$8.68 \cdot 10^{-12}$	7.09661	96.16559	4.24662	0.89918	$3.98 \cdot 10^{-10}$	$1.13 \cdot 10^{-11}$
2	$7.01 \cdot 10^{-12}$	7.17359	159.27710	4.37142	0.87314	$9.85 \cdot 10^{-10}$	$3.57 \cdot 10^{-11}$
2.01	$8.46 \cdot 10^{-12}$	7.19204	190.69520	4.40270	0.86565	$8.81 \cdot 10^{-11}$	$1.12 \cdot 10^{-10}$
2.02	$9.30 \cdot 10^{-12}$	7.21025	237.78943	4.43405	0.85773	$6.09 \cdot 10^{-10}$	$2.09 \cdot 10^{-11}$
2.03	$3.76 \cdot 10^{-11}$	7.22827	316.28491	4.46550	0.84937	$1.27 \cdot 10^{-09}$	$5.64 \cdot 10^{-10}$
2.04	$8.83 \cdot 10^{-11}$	7.24614	473.44293	4.49709	0.84056	$5.24 \cdot 10^{-09}$	$7.52 \cdot 10^{-10}$
2.05	$8.71 \cdot 10^{-10}$	7.26391	946.52061	4.52884	0.83129	$5.46 \cdot 10^{-08}$	$5.07 \cdot 10^{-09}$
2.055	$8.08 \cdot 10^{-09}$	7.27277	1899.810	4.54478	0.82648	$8.54 \cdot 10^{-07}$	$3.93 \cdot 10^{-08}$

Table 4. Values of relevant parameters for $b > 1.8$ in second-kind solutions. When $b \leq 2$ ($b > 2$) the calculations were performed using $400(10^3)$ Chebyshev points.

and $x(1) = 6.841203\dots$, already found and listed in Table 2, the minimization algorithm, just in its simplest implementation, converges [see Figs. 9 and 10] to a new profile, uniformly smaller than $\xi_F(s, b_1)$ and therefore with the larger normalization factor $K = 6.692666\dots$ and a larger size $x(1) = 35.119263\dots$

Having obtained a new, or second-kind, solution for $b = 1.8$, we can now proceed and progressively reduce b toward b_1 , using as starting point of a new run the final profile of the preceding successful run. This should imply a uniform increase in $\xi_F(s)$, with a corresponding decrease in K , but always remaining above $K(b_1)$, the value of K that separates the two branches. Albeit slow, this procedure indeed works as expected, with the results listed in Table 3 (it is actually too slow to reach the value $b = 1.6314932$, probably because the other first-kind solution is too close). Notice that only the minimization algorithm works successfully, since the iterated map always falls back to a solution of the first kind with $K < K(b_1)$. In other words the second-kind solution at a given b represents an unstable fixed point of the iterated map (4.12). We can verify this by looking at the eigenvalues of the Jacobian matrix $J(1)$ in eq. (4.13). We find that the largest eigenvalue now exceeds one, while there are eigenvalues with negative real part. This means that no choice of α would make the iterated map (4.12) convergent.

To try and complete the branch of solutions of the second kind, we next progressively increase b from the value 1.8. Now K and $x(1)$ increase with b , with the size $x(1)$ increasing very fast for $b \gtrsim 2$. The rise of $x(s)$ as $s \rightarrow 1$ becomes so steep that it can compromise the accuracy of the calculation of the integral transform (4.4) when using $N = 400$ Chebyshev points, even if the free parameter h is tuned to absorb as much as possible the growth in the prefactor $(1 - hs)^{-1}$, according to eqs. (3.1). Notice that one cannot move h too close to

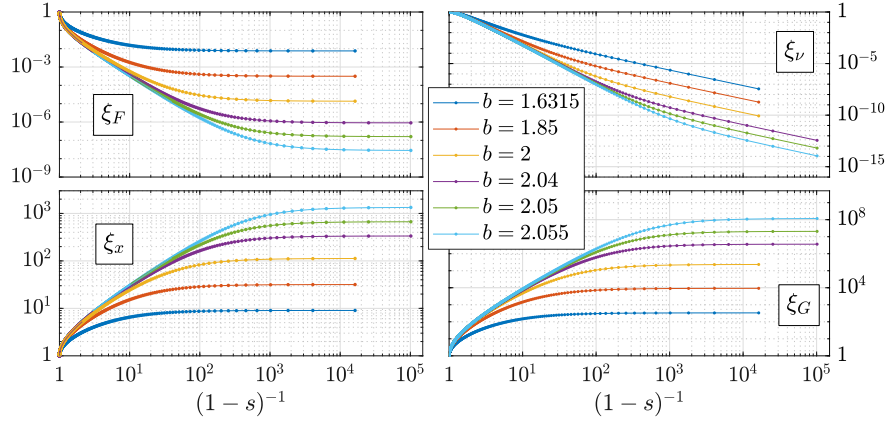


Figure 11. Second-kind ξ_F , ξ_ν , ξ_x and ξ_G at selected values of b . These are profiles with $h = 0$ in eqs. (2.19), (2.20) and (3.1), although in the actual calculations h was set to values growing with b towards 1, to absorb as much as possible the large growth of ξ_x and ξ_G . The profiles corresponding to the three smaller values of b are defined over the grid with $N = 400$ points, while the other three are defined over the grid with $N = 1000$.

unity, or $\xi_F(s)$ would develop a steep rise as $s \rightarrow 1$, which would in turn lower the quality of the Chebyshev approximation of the other integral transform (4.3). For this reason we use also $N = 1000$ Chebyshev points for all values $b > 2$ where we search for solutions.

The results for some specific values of b are listed in Table 4, while some of the profiles are plotted in Fig. 11. Evidently, for $b \gtrsim 2$ the accuracy progressively worsen. As discussed in the Appendix, this is due to the second step in the chain (2.14), that is Poisson's equation (2.3), because of the increasing span of its solution $x(u)$. Although the bound (4.11) on the residuals is not satisfied for the last three entries of the table, relying on the continuity in b we can still regard them as adequate, if not fully accurate, numerical solutions.

The solutions of the second kind belong to a family continuous in b , with the prominent feature that

$$\xi_F(s, b) > \xi_F(s, b'), \quad \forall s \in [0, 1], \quad \text{if } b < b', \quad (5.2)$$

which is a behavior opposite w.r.t. the first kind [see eq. (5.1)]. Another, even more prominent feature of this second-kind family is the existence of a value $b = b_2$ where the dimensionless size $x(1)$ diverges. We can find an approximate value of b_2 by fitting $1/x(1)$ vs. b . Using the six values of $x(1)$ listed in Table 4 for $b > 2$ (obtained with the more accurate setup based on $N = 1000$ Chebyshev points) we consider the polynomial interpolations of $1/x(1)$ vs. b from degree one to five (with centering and scaling for the higher degrees). The root of each polynomial which is closest to $b = 2.055$ provides an approximate value of b_2 . We find

degree of polynomial	b_2	max residual
1	2.0600857	$1.418 \cdot 10^{-5}$
2	2.0599539	$3.975 \cdot 10^{-7}$
3	2.0599476	$9.948 \cdot 10^{-8}$
4	2.0599507	$6.046 \cdot 10^{-9}$
5	2.0599511	$1.697 \cdot 10^{-18}$

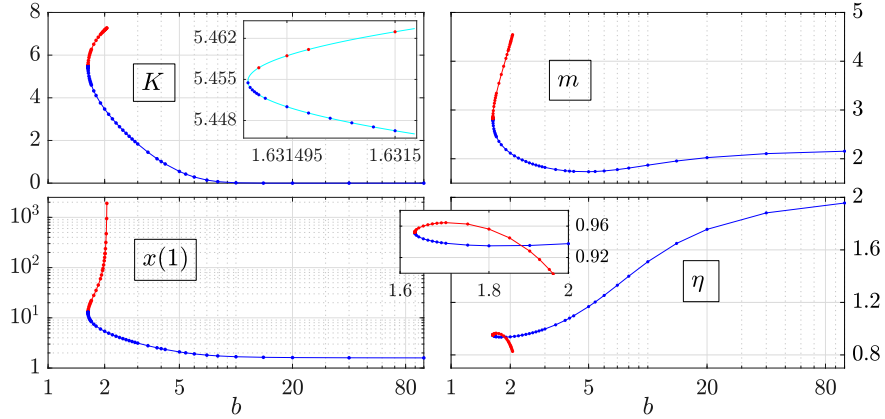


Figure 12. Plot of K , $x(1)$, m and η vs. b . The dots (blue for first-kind solutions and red for second-kind solutions) mark where the calculation was performed. The continuous cyan curve in the inset of the upper right panel is the parabolic fit to the actual data marked by the dots.

This calculation is stable and shows that $x(1)$ diverges as $(b_2 - b)^{-1}$ as $b \rightarrow b_2$. Moreover, the profiles in Fig. 11 show the emergence, as $b \rightarrow b_2$, of scaling windows where ξ_F , ξ_ν , ξ_x and ξ_G have near $s = 1$ the power behavior characteristic of infinite-size systems, as discussed in subsection 2.1.

We do not know whether the second-kind family continues beyond b_2 with $x(1)$ infinite but b -dependent mass and temperature. Unfortunately, we cannot solve Poisson's equation (2.3) with the necessary accuracy when $\lim_{u \rightarrow 1} x(u) = \infty$.

5.3 A unifying view of the two kinds of solutions

In Fig. 12 we plot K , $x(1)$, m and η vs. b , considering both families of solutions. Obviously, for $b_1 < b < b_2$ these quantities are all double-valued as functions of b . Viceversa, b is a single-valued function of K and of $x(1)$, while it is double-valued as function of m or of η . Near the lowest value b_1 , say for $b \leq 1.6315$, b itself is very well approximated, as a function of K , $x(1)$, m or η , by a parabola. In the inset in the upper left panel of Fig. 12 we show this fit in the case of b vs. K . These fits allow accurate approximations for b_1 as the minimum of each parabola. Actually, better accuracy is obtained by using third order polynomials rather than parabolas (clearly b is not even as function of K , $x(1)$, m or η). We find

variable	b_1	value at b_1	max residual
K	1.63149319330	5.45468873434	$4.14 \cdot 10^{-11}$
$x(1)$	1.63149319327	12.7191519275	$1.176 \cdot 10^{-10}$
m	1.63149319329	2.82245779594	$5.14 \cdot 10^{-11}$
η	1.63149319328	0.95194462704	$1.093 \cdot 10^{-10}$

Taking into account that 10^{-11} is the accuracy of both solution families, we conclude that

$$b_1 = 1.631493193(3) . \quad (5.3)$$

The parameter b is just a Lagrange multiplier and, after computing the physical observables, it can be eliminated in favor of one such observable; the dimensionless size $x(1)$ is

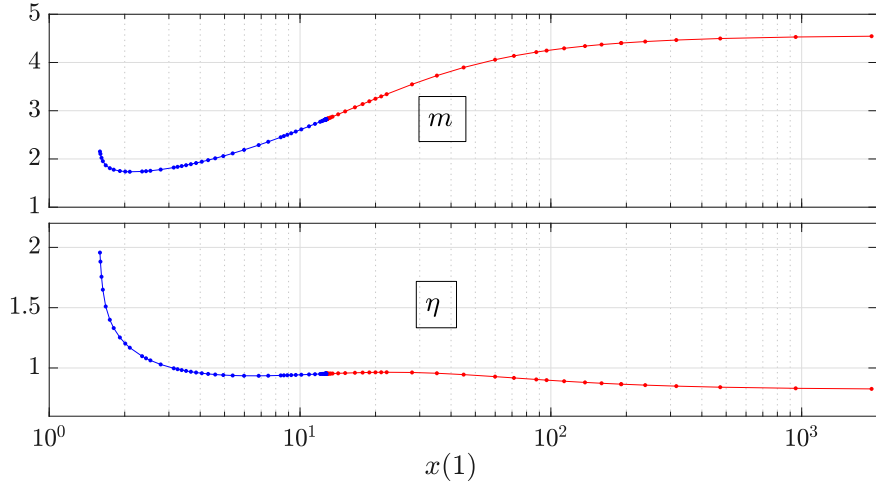


Figure 13. Plot of m and η vs. $x(1)$. Again, blue(red) dots mark actual calculations for solutions of the first (second) kind.

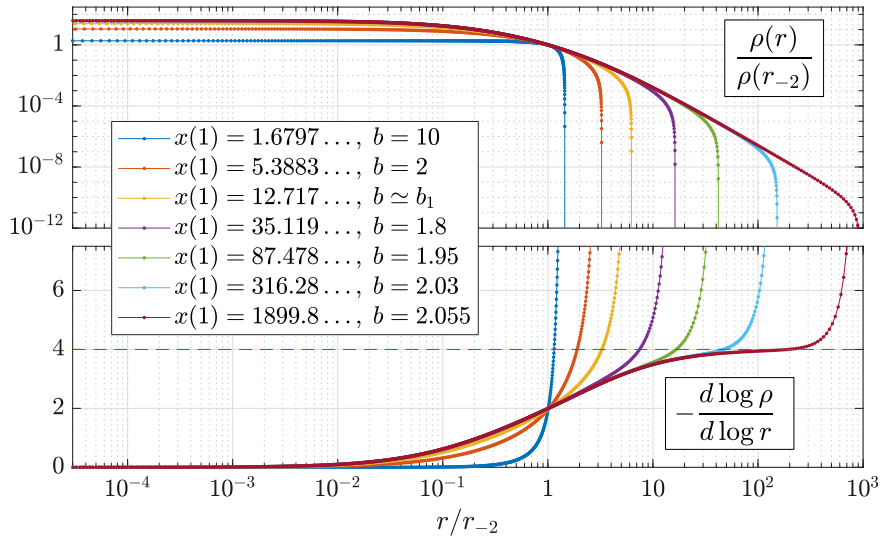


Figure 14. The density profiles (upper panel) and their logarithmic slopes (lower panel) for few selected solutions; the first three are from the family of the first kind and the last four from that of the second kind.

clearly the best choice. In Fig. 13 we plot the dimensionless mass m and temperature η vs. $x(1)$. No particular feature highlights the transition from the family of the first kind to the second-kind family. Such transition is evident only because of the different colors used in the plots. Similarly, the four profiles ξ_F , ξ_ν , ξ_x and ξ_G have a smooth and regular dependence on $x(1)$: ξ_F and ξ_ν monotonically and uniformly decrease as $x(1)$ grows, while ξ_x and ξ_G monotonically and uniformly increase.

A very important profile is that of $\rho(r)$, the mass density vs. the radius. In Section 2, to fix the distance scale we used r_* , which relates the central density ρ_0 (a local quantity) to

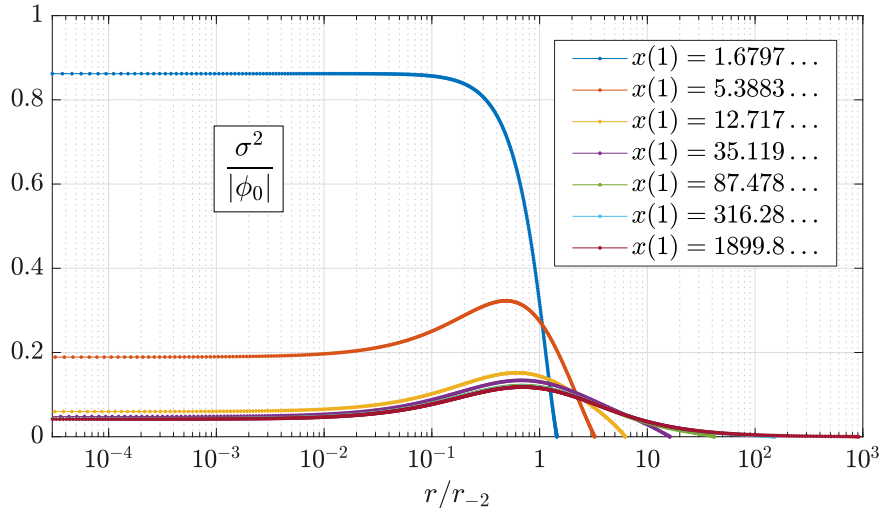


Figure 15. The squared velocity dispersion for the same selected solutions of Fig. 14.

the total mass M (a global quantity) as in eq. (2.11). Another, fully local scale, denoted r_{-2} , is often used. It is defined as the largest radius at which the logarithmic slope $r\rho'(r)/\rho(r)$ takes the value -2 . In the upper panel of Fig. 14 we plot several profiles of $\rho(r)/\rho(r_{-2})$ vs. r/r_{-2} . Again, nothing special happens at the transition from the first- to the second-kind family. Notice also the emergence of the r^{-4} law at large distances when b approaches b_2 , as evident also from the logarithmic slopes plotted in the lower panel.

Finally, in Fig. 15 we plot the squared velocity dispersion [see eqs. (2.23) and (2.26)] for the same cases of Fig. 14. It is evident as these cored DARKexp systems get cooler as their size grows.

5.4 Asymptotic fit

In the Appendix we present an a priori analysis on the accuracy of our numerical results, with a typical estimate of order 10^{-11} . In this section we check the numerical accuracy against the only exact analytical result that we know, that is the next-to-leading asymptotics (3.2) derived in [47].

In principle, having computed the Chebyshev approximation (4.2) for the four functions ξ_F , ξ_ν , ξ_x and ξ_G , to compute the first correction of order $u^{-1/2}$ in eq. (3.2) we could just evaluate the second derivative of $\xi(z^4)$ w.r.t. z at $z = 0$. This procedure is however quite inaccurate, due to the intrinsic nature of polynomial interpolations, which in our case is aggravated by the expected presence of a singular logarithmic correction. A better procedure, which allows to estimate also the coefficient of logarithmic correction, is to use a finite version of the expansion (3.3) to fit our numerical $\xi(s)$ over a small subinterval $[0, d]$, with $d \ll 1$ suitably chosen to maximize the reliability of the fit. For small enough d only relatively few coefficients in the expansion are numerically relevant and any non-linear least-squares method [for instance the Levenberg–Marquardt algorithm already at work with eq. (2.21)] converges very quickly. Initially we can pick d so small that N_d , the number of grid points in $[0, d]$ (that is the number of values to be fitted), is not much larger than M_d , the number of relevant coefficients. Then d could be increased as long as the fit improves, reducing the

b	$x(1)$	d	M_d	N_d	RM_d/N_d	$ 1 - b_F $	$ 1 - a_F $
5	2.096	$3.2 \cdot 10^{-7}$	8	40	$3.69 \cdot 10^{-13}$	$8.87 \cdot 10^{-9}$	$2.77 \cdot 10^{-3}$
2	5.388	$3.2 \cdot 10^{-7}$	8	40	$5.25 \cdot 10^{-14}$	$3.82 \cdot 10^{-9}$	$1.93 \cdot 10^{-4}$
1.6315	12.660	$8.0 \cdot 10^{-8}$	8	34	$1.16 \cdot 10^{-14}$	$1.13 \cdot 10^{-9}$	$7.06 \cdot 10^{-5}$
b_1	12.717	$8.0 \cdot 10^{-8}$	8	34	$1.14 \cdot 10^{-14}$	$9.39 \cdot 10^{-10}$	$6.32 \cdot 10^{-5}$
1.6315	12.779	$1.6 \cdot 10^{-7}$	8	37	$4.98 \cdot 10^{-14}$	$3.05 \cdot 10^{-9}$	$9.58 \cdot 10^{-5}$
2	159.277	$8.0 \cdot 10^{-8}$	8	34	$4.85 \cdot 10^{-14}$	$1.14 \cdot 10^{-9}$	$6.71 \cdot 10^{-5}$
2.03	316.285	$3.2 \cdot 10^{-7}$	8	99	$1.25 \cdot 10^{-13}$	$6.92 \cdot 10^{-9}$	$1.68 \cdot 10^{-4}$
2.05	946.521	$3.2 \cdot 10^{-7}$	8	99	$1.29 \cdot 10^{-13}$	$7.08 \cdot 10^{-9}$	$1.69 \cdot 10^{-4}$
2.055	1899.811	$5.1 \cdot 10^{-6}$	8	141	$1.88 \cdot 10^{-10}$	$1.87 \cdot 10^{-6}$	$4.14 \cdot 10^{-3}$

Table 5. Asymptotic fit of $\xi_F(s)$ to eq. (3.3), with numerical check of the exact relations in eq. (5.4).

least-square residuals multiplied by the ratio M_d/N_d .

An obvious limitation applies to the very compact solutions where $K \ll 1$, since the numbers we want to check are, for instance in the case of $\xi = \xi_F$,

$$b_F = -\frac{45b_{F,00}}{32K}, \quad a_F = -\frac{45a_{F,10}}{2K^2}. \quad (5.4)$$

According to eq. (3.2) these should both take the value 1 in any solution, irrespective of b and of the family kind. Clearly accuracy is lost when $K \ll 1$ and b_F , a_F are ratios of very small numbers.

The results of our asymptotic fit are listed in Table 5 for a selected set of numerical solutions. We only consider a_F and b_F , since the other three cases, when F is replaced by ν , x or G , yield very similar results. Keeping into account the intrinsic weakness of this kind of fit, the agreement of numbers vs. analytics is extremely good for b_F . The lower level of agreement for a_F is to be expected, due to the singular nature of the log.

6 Discussion and outlook

In this work we have numerically computed very accurate solutions of the DARKexp problem, namely, we calculated ergodic phase-space distribution functions $f(E)$ that determine the DARKexp differential energy distribution $n(E)$ given by eq. (1.1). We have assumed cored density profiles, by imposing the asymptotic condition $f(E) \sim (E - \phi_0)^{-1}$ near the bottom of the potential well. As a consequence, beside ϕ_0 , we have the density ρ_0 in the origin as second free parameter fixing the two scales of the problem. Together with the choice $4\pi G = 1$, we thus obtain a fully dimensionless formulation, described in section 2, in which the energy space is mapped in the unit interval and $f(E)$ is proportional to a function $F(s)$ over such interval which parametrically depends on the dimensionless Lagrange multiplier $b = \beta\phi_0$. Beside being very accurate (typically to order 10^{-10}), our solution is complete, in the sense that it holds throughout the unit interval, with the integral transforms connecting $F(s)$ to $G(s)$, the dimensionless version of the density of states $g(E)$, numerically computed to high accuracy without any reduction of the integration interval. This is possible thanks to the reformulation (2.3) of Poisson's equation, in which the radial coordinate becomes the unknown to be determined over the span of the gravitational potential (also mapped to the unit interval). The price to be paid is that only systems with a finite size can be computed in this way, if high accuracy at any distance is to be preserved.

Our numerical results substantially differ from those reported in [45]. Lacking any detailed description of the numerical approach adopted in [45], we can only make some educated guess on the reasons for such manifest discrepancy. First of all, our numerical method is grounded on the assumption of core density profiles, while the numerical results in [45] are claimed to correspond to $1/r$ cusps. It is well possible that DARKexp admits many different solutions, both cored and cusped. In fact, the shape parameter in [14], where the DARKexp models was first put forward, is $\beta\Phi(0)$ and in the numerics of [45] it takes the values 2.0, 4.0, 2.83, 4.0, 5.66 and 8.0. It is related to our shape parameter b as

$$\beta\Phi(0) = \left[1 + \frac{m}{x(1)}\right]b.$$

Since for the second-kind solutions we have $b < b_2 = 2.0599\dots$, we see that the two parametrizations really overlap only when we consider the first-kind solutions, those with small size. Namely, for the same value of β , with $\beta\Phi(0) \geq 2$, we have a cored density profile with rather small size (see Fig. 14), whereas a density with a much larger size that oscillates at short distances around the NFW profile is found in [45]. Most likely, two different solutions are found because the iterative numerical method of [46] is used in [45] starting from the NFW profile itself, while in our numerical approach we start from a cored, finite size profile.

To clarify this matter, we should try and extend our accurate numerical approach to cusped systems. However, this extension is not so straightforward if one wants to preserve high accuracy throughout energy space, since the phase-space distribution of $1/r$ -cusped system diverges as $(E - \phi_0)^{-5/2}$ near the bottom of the potential well. We suspect that this strong divergence, if not properly treated, might introduce numerical artifacts even when the iterated map happens to converge. Further work is necessary in this direction.

As we anticipated in the Introduction, we do not try here to apply our findings to realistic self-gravitating systems. In fact, ergodic phase-space distributions have by themselves a limited applicability to the outcome of real collapses, where angular momentum plays a crucial role also in case of perfect spherical symmetry. Our goal in this work, as in the preceding one [47], was to develop a framework, both analytic and numeric, for a trustworthy and accurate solution of the DARKexp problem, since we regard the DARKexp model as a well founded first-principle approach to the quasi-equilibrium of collisionless self-gravitating matter, which moreover happens to be compatible with observations and N -body simulations. We have found here a novel family of ergodic systems with finite size, mass and energy and with a cored density profile. They match very well the analytic results of [47] and have interesting physical properties summarized in Figs. 14 and 15. We leave for the future the development of all the extensions and modifications which are necessary to try and apply these ideas to realistic systems.

A Accuracy checks and algorithmic details

We present here an analysis of the accuracy of the numerical results described in section 5, providing at the same time more details on the calculations. These were all performed in MATLAB R2017b with the help of the Chebfun package [50] on a workstation Dell T7600.

Let us first examine the accuracy of our approach to the integral transforms in eqs. (2.7) and (2.12). Given a choice of N , the two $(N + 1) \times (N + 1)$ matrices $I^{(F\nu)}$ and $I^{(xG)}$ [see eqs.(4.5), (4.6) and (4.9)] can be computed once and for all to any desired accuracy

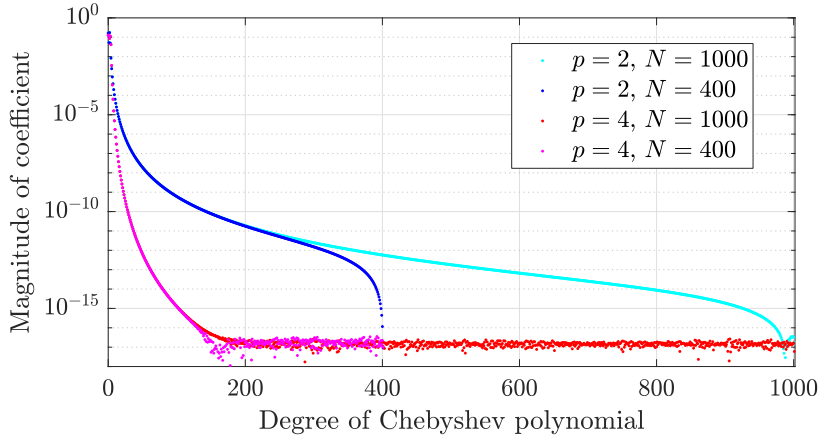


Figure 16. Comparison of the decay of the Chebyshev coefficients of the test function $z^p \log z^p$ for $p = 2$ and $p = 4$ when $N = 400$ or $N = 1000$ Chebyshev point are used.

with a suitable quadrature tool. We used the `quadgk` routine in MATLAB with 10^{-12} as tolerance, both absolute and relative. Typically, for smooth integrands such as those in eqs.(4.5) and (4.9), the accuracy is much better than the tolerance, that is to say, the numerical results differ from known analytic ones by much less than 10^{-12} .

However, the accuracy on the full integrals in eqs. (4.3) and (4.4) could be much worse, and even much larger than 10^{-12} , depending on the quality of the Chebyshev approximation (4.2) for $\xi_F(z^p)$ and $[\xi_x(z^p)]^3$. This quality is measured by the decay rate of the corresponding Chebyshev coefficients and can be assessed at the end the calculation. Given the coefficients, the simplest way to infer the overall accuracy is to test our quadrature procedure on known test functions replacing $K\xi_F(s)$ and $\xi_x(u)$ in eqs. (4.3) and (4.4).

The analytic results in eq. (3.2), which already suggested the reparametrization $s = z^p$, with p even to make the leading term $\propto s^{1/2}$ analytic, now suggest also $s \log s$ as test function. With $p = 2$ one obtains first order differentiability in $z = 0$ and a sub-optimal behavior of the Chebyshev coefficients, while with $p = 4$ one gets differentiability up to third order in $z = 0$ and very fast convergence of the coefficients below machine ϵ as shown in Fig. 16. The “exact” integrations to be used as reference are

$$I_1(u) = \frac{1}{3} \int_u^1 ds \frac{s \log s}{s} (s - u)^{1/2} = \frac{4}{9} \left[\frac{1}{3}(4u - 1)(1 - u)^{1/2} - u^{3/2} \arctan(u^{-1} - 1)^{1/2} \right]$$

and

$$I_2(s) = \frac{8}{3\pi s^2} \int_0^s du (u^{3/2} \log u)^3 (s - u)^{-1/2}.$$

In the case of $I_2(s)$ we do not write nor use the analytic expression, which could nonetheless be obtained, but rather compute the integral numerically at the grid values of u with the help of MATLAB’s `integral` routine, using 10^{-14} as absolute as well as relative tolerance.

We verified that, upon the action of the matrices $I^{(F\nu)}$ and $I^{(xG)}$ over the coefficient vectors of $z^p \log z^p$ as in eqs. (4.6) and (4.9), one obtains, if $N = 10^3$, accuracies to order 10^{-14} when $p = 2$ and even better when $p = 4$, practically to the limits of any computation in double precision. On the other hand, if $N = 400$, only with $p = 4$ this high accuracy is preserved, while it gets worse by almost two orders of magnitude when $p = 2$. This is still

$x(1)$	a	$x^{(I)}(a)$	$x^{(II)}(a)$	$\Delta^{(I,400)}$	$\Delta^{(II,400)}$	$\Delta^{(I,1000)}$	$\Delta^{(II,1000)}$
5.388	0.700	3.8006	8.6581	$1.18 \cdot 10^{-12}$	$1.96 \cdot 10^{-12}$	$8.18 \cdot 10^{-13}$	$2.21 \cdot 10^{-12}$
12.703	0.875	8.4853	21.8967	$1.31 \cdot 10^{-12}$	$3.76 \cdot 10^{-12}$	$4.28 \cdot 10^{-12}$	$2.19 \cdot 10^{-12}$
159.277	0.985	67.1648	187.8520	$1.96 \cdot 10^{-11}$	$1.07 \cdot 10^{-10}$	$9.34 \cdot 10^{-12}$	$2.42 \cdot 10^{-10}$

Table 6. Accuracy checks in the case of the two analytic solutions of Poisson’s equation in eqs. (A.1) and eqs. (A.2).

very accurate, since after all the Chebyshev coefficients of $z^2 \log z^2$ with index larger than 400 are smaller than 10^{-12} , but the quality of our approach can only worsen in the true calculations with $\xi_F(z^p)$ and $[\xi_x(z^p)]^3$. Hence our choice of $p = 4$ in the actual computations whose results are reported in section 5, with confidence that a behavior of the Chebyshev coefficients of $\xi_F(z^p)$ and $[\xi_x(z^p)]^3$ similar to those of the test functions should guarantee a comparable accuracy in the integrations (4.3) and (4.4).

The second step $\nu \rightarrow x$ in the chain (2.14), which we implement by numerically solving Poisson’s equation in the form eq. (4.7), is by far the most time-consuming in the chain (2.14). We used the ODE solvers `ode45` and `ode113` in MATLAB, with an absolute tolerance of 10^{-15} and a relative tolerance ranging from 10^{-6} down to 10^{-12} . The relative tolerance controls in particular the accuracy near the initial conditions for $\gamma(y)$ and therefore affects the accuracy everywhere else, in particular near $s = 1$. Comparing solutions at different relative tolerances allows to estimate this accuracy. Another check is possible by comparing the numerical solution to analytic ones, such as the Schuster model (a.k.a. Plummer’s model or $n = 5$ polytrope system), which in our dimensionless setup is written, with $h = 1$ in eq. (3.1),

$$\xi_\nu^{(I)}(u) = (1 - u)^5, \quad \xi_x^{(I)}(u) = (1 - u/2)^{1/2}. \quad (\text{A.1})$$

Another possibility is, still with $h = 1$,

$$\xi_\nu^{(II)}(u) = (1 - u^{1/2})^4, \quad \xi_x^{(II)}(u) = 1 + u^{1/2}. \quad (\text{A.2})$$

These two analytic solutions of Poisson’s equation (2.3) have infinite size, with the dimensionful density $\rho(r)$ dying off at large r as r^{-5} and r^{-4} , respectively. Our numerical approach is not set up to deal with infinite size with the necessary accuracy, hence we restrict the u -interval to $[0, a]$ with a slightly less than 1. By varying a we can check the accuracy of the numerical solution of eqs. (2.3) [in the equivalent form (4.7)] by fixing a so that $x^{(I)}(a) \approx x(1)$ or $x^{(II)}(a) \approx x(1)$ for anyone of the solutions described in section 5. Notice that in the tests the ODE solver does not use the known analytic forms of $\xi_\nu^{(I)}(u)$ or $\xi_\nu^{(II)}(u)$, but their N -order Chebyshev interpolations based on the values they assume on the N points defined by eq. (4.1).

Let us define, for $J = I, II$ and $N = 400, 1000$, the absolute error of the numerical solution of eq. (4.7) w.r.t. the exact analytic solution

$$\Delta^{(J,N)} = \max_s |\xi_x^{(J,N)}(s) - \xi_x^{(J)}(s)|.$$

We find the results listed in Table 6. As expected, $\Delta^{(J,N)}$ strongly depends on the scale of $x^{(I)}(a)$ or $x^{(II)}(a)$. We infer that a similar accuracy holds for the ξ_x of section 5 w.r.t. the unknown exact solution. In particular we see that when $b > 2$ in the family of solutions of the second kind, that is when $x(1) > 159.2771\dots$, the overall accuracy of the calculation is

entirely determined by the accuracy of the second step $\nu \rightarrow x$ in the chain (2.14), that is by Poisson’s equations.

Let’s now come the part of the calculation that drives the integrations and the ODE solver, that is the solution of eq. (2.21). We have reduced the problem to a system of N non-linear equations for the N unknowns $\xi_F(z_k^p)$, $k = 1, 2, \dots, N$, to be dealt with with either one, or possibly both, of the two approaches described in subsection 4.2. There is little to say about the iterative scheme (4.12), which has only one tunable parameter, the damping factor α . The best case if it converges for $\alpha = 1$, as it happens for the solutions of the first kind of subsection 5.1. If not, as in the case of the second-kind family of subsection 5.2, one could in principle try few other values of order one, both positive and negative. However, if the Jacobian matrix $J(1)$ [see eq. (4.13)] has eigenvalues with magnitude larger than one, there is a little chance to gather all eigenvalues of $J(\alpha)$ within the unit circle just by varying α . In fact, this failure just characterizes the second-kind solutions. In these circumstances, it is necessary to use algorithms that minimize a suitable objective function, such as $\mathcal{F}[\xi_F]$ in eq. (4.14). Through the Optimization Toolbox, MATLAB offers the specific function `fsolve` for this purpose. As other functions of that toolbox, `fsolve` has a wealth of options that can be fixed to improve the overall behavior of the routine. One such option chooses the actual minimization algorithm. We found the Levenberg–Marquardt algorithm to be very efficient for our problem and used it most of the times.

Besides the precise form of the objective function, which can be changed for instance by varying the weights w_k , one can vary also the parametrization of the step in ξ_F . We mostly used the following, positive-definite and very simple form

$$\xi_F(z_k^p) = \xi_F^{(0)}(z_k^p) \exp(y_k), \quad k = 1, 2, \dots, N,$$

where $\xi_F^{(0)}$ is the initial configuration and the y_k are the numbers which are varied in the Levenberg–Marquardt algorithm. Sometime we found it necessary to use also another parametrization, based on the expansion (3.3).

Other important options in `fsolve` are the *FunctionTolerance* and the *StepTolerance*, which can be fixed to values small enough to obtain the required accuracy when the algorithm eventually stops, because the objective function does not decrease enough any more (*FunctionTolerance*) or the proposed change in ξ_F is too small (*StepTolerance*). The final ξ_F is an acceptable solution of eq. (2.21) if it satisfies the criterion (4.11).

A confirmation that $\epsilon = 10^{-11}$ is indeed close to the limits of the double-precision accuracy for this kind of computations is drawn from the typical profile of the magnitude of the residuals R_k in a successful run [see Fig. 3]. This profile is dominated at small z by the rugged patterns characteristic of roundoff errors. Notice that any numerical error at low z is inevitably amplified at higher z by the ODE solver in the $\nu \rightarrow x$ step. In fact, for more compact systems where $x(u)$ has a smaller variation, we can obtain $|R_k|$ much smaller than 10^{-11} and rugged almost throughout the interval $[0, 1]$. Another independent confirmation of the $\epsilon = 10^{-11}$ rule comes from the behavior of the maximal residual \mathcal{R} in the iterated map (4.12), as evident from Figs. 1 and 8.

Quite naturally, there could be also unsuccessful runs of `fsolve`, since the Levenberg–Marquardt algorithm, as any other local minimization algorithm, may eventually stop at some ξ_F that is not a solution of eq. (2.21). This could happen for two reasons: eq. (2.21) itself simply has no solution for the specific value of b one is considering, or $\xi_F^{(0)}$, the starting point passed to the algorithm, is in the basin of attraction of a local minimum of the objective

function which is not its global minimum. In the latter case the iterative approach (4.12) might help to get away from the local minimum and move toward an acceptable solution. At any rate, as stated near the end of subsection 4.2, we cannot consider a failure to produce an acceptable solution through our numerical methods as a rigorous proof of non-existence of the exact, infinite-precision solution for the given value of b . But it certainly is strong indication of non-existence.

The last question concerns the accuracy of an acceptable solution w.r.t. the exact solution. Taking into account the accuracies in the various steps of the calculation, as discussed above, we are confident that such a solution is accurate to at least 10^{-10} , provided the Chebyshev coefficients of ξ_F and ξ_x^3 decay rapidly enough towards zero, in a way similar to that in Figs. 16 or 4. This we verified for all our numerical solutions. The only exceptions to the 10^{-10} accuracy rule are the last four cases of table 4, because of the worse accuracy in the solution of Poisson's equation. In these cases, an estimate of the overall accuracy is provided by Δm and $\Delta \eta$ in the same table.

Acknowledgments

The author acknowledges the contribution of Michele Turelli in the very early stages of this work.

References

- [1] W. Braun and K. Hepp, *The Vlasov dynamics and its fluctuations in the $1/N$ limit of interacting classical particles*, *Commun. Math. Phys.* **56** (1977) 101.
- [2] P.H. Chavanis, *Hamiltonian and Brownian systems with long-range interactions: III. The BBGKY hierarchy for spatially inhomogeneous systems*, *Physica A* **387** (2008) 787.
- [3] J. Binney and S. Tremaine, *Galactic Dynamics*, Princeton Univ. Press, Princeton (2008).
- [4] T. Padmanabhan, *Statistical mechanics of gravitating systems*, *Phys. Rep.* **188** (1990) 289.
- [5] S. J. Aarseth, *Gravitational N-Body Simulations: Tools and Algorithms*, Cambridge Univ. Press, Cambridge (2003).
- [6] J.F. Navarro *et al.*, *The diversity and similarity of simulated cold dark matter haloes*, *Mon. Not. Roy. Astron. Soc.* **402** (2010) 21.
- [7] D. Lynden-Bell, *Statistical mechanics of violent relaxation in stellar systems*, *Mon. Not. Roy. Astron. Soc.* **136** (1967) 101.
- [8] M. Stiavelli and G. Bertin, *Statistical mechanics and equilibrium sequences of ellipticals*, *Mon. Not. Roy. Astron. Soc.* **229** (1987) 61.
- [9] S.D.M. White and R. Narayan, *Maximum entropy states and the structure of galaxies*, *Mon. Not. Roy. Astron. Soc.* **229** (1987) 103.
- [10] J. Hjorth and J. Madsen, *Violent relaxation and the $R \propto 1/4$ law*, *Mon. Not. Roy. Astron. Soc.* **253** (1991) 703.
- [11] D.N. Spergel and L. Hernquist, *Statistical mechanics of violent relaxation*, *Astrophys. J.* **397** (1992) L75.
- [12] A.R. Plastino and A. Plastino, *Stellar polytropes and Tsallis' entropy*, *Phys. Lett. A* **174** (1993) 384.

- [13] P.H. Chavanis and J. Sommeria, *Degenerate equilibrium states of collisionless stellar systems*, *Mon. Not. Roy. Astron. Soc.* **296** (1998) 569.
- [14] J. Hjorth and L.L.R. Williams, *Statistical mechanics of collisionless orbits. I. Origin of central cusps in dark-matter halos*, *Astrophys. J.* **722** (2010) 851.
- [15] P. He and D.B. Kang, *Entropy principle and complementary second law of thermodynamics for self-gravitating systems*, *Mon. Not. Roy. Astron. Soc.* **406** (2010) 2678.
- [16] A. Pontzen and F. Governato, *Conserved actions, maximum entropy and dark matter halos*, *Mon. Not. Roy. Astron. Soc.* **430** (2013) 121.
- [17] J.F. Navarro JF, V.R Eke VR, C.S. Frenk (1996) *The cores of dwarf galaxy haloes*, *Mon. Not. Roy. Astron. Soc.* **283** (1996) L72.
- [18] F. Governato, A. Zolotov, A. Pontzen, C. Christensen, S. H. Oh, A. M. Brooks, T. Quinn, S. Shen and J. Wadsley, *Cuspy no more: How outflows affect the central dark matter and baryon distribution in Λ CDM galaxies.*, *Mon. Not. Roy. Astron. Soc.* **422** (2012) 1231.
- [19] A. Pontzen and F. Governato, *How supernova feedback turns dark matter cusps into cores*, *Mon. Not. Roy. Astron. Soc.* **421** (2012) 3464.
- [20] T.K. Chan, D. Kereš, J. Oñorbe, P.F. Hopkins, A.L. Muratov, C.-A. Faucher-Giguère and E. Quataert, *The impact of baryonic physics on the structure of dark matter haloes: the view from the FIRE cosmological simulations*, *Mon. Not. Roy. Astron. Soc.* **454** (2015) 2981.
- [21] A.M. Brooks, E. Papastergis, C.R. Christensen, F. Governato, A. Stilp, T.R. Quinn and J. Wadsley, *How to Reconcile the Observed Velocity Function of Galaxies with Theory*, *Astrophys. J.* **850** (2017) 97.
- [22] D.N. Spergel and P.J. Steinhardt, (2000) *Observational evidence for self-interacting cold dark matter*, *Phys. Rev. Lett.* **84** (2000) 3760.
- [23] M. Vogelsberger, J. Zavala and A. Loeb, *Subhaloes in self-interacting galactic dark matter haloes*, *Mon. Not. Roy. Astron. Soc.* **423** (2012) 3740.
- [24] M. Rocha, A.H.G. Peter, J.S. Bullock, M. Kaplinghat, S. Garrison-Kimmel, J. Oñorbe and L.A. Moustakas, *Cosmological simulations with self-interacting dark matter - I. Constant-density cores and substructure*, *Mon. Not. Roy. Astron. Soc.* **430** (2013) 81.
- [25] J. Zavala, M. Vogelsberger and M.G. Walker, *Constraining self-interacting dark matter with the Milky Way's dwarf spheroidals*, *Mon. Not. Roy. Astron. Soc.* **431** (2013) L20.
- [26] M. Vogelsberger, J. Zavala, F. Cyr-Racine, C. Pfrommer, T. Bringmann and K. Sigurdson *ETHOS - an effective theory of structure formation: dark matter physics as a possible explanation of the small-scale CDM problems*, *Mon. Not. Roy. Astron. Soc.* **460** (2016) 1399.
- [27] S. Colombi, S. Dodelson, and L. M. Widrow, *Large-Scale Structure Tests of Warm Dark Matter*, *Astrophys. J.* **458** (1996) 1.
- [28] P. Bode, J. P. Ostriker, and N. Turok, *Halo Formation in Warm Dark Matter Models*, *Astrophys. J.* **556** (2001) 93.
- [29] M. Viel, G. D. Becker, J. S. Bolton, and M. G. Haehnelt, *Warm Dark Matter as a solution to the small scale crisis: new constraints from high redshift Lyman- α forest data*, *Phys. Rev. D* **88** (2013) 043502.
- [30] C. J. Hogan and J. J. Dalcanton, *New dark matter physics: Clues from halo structure* *Phys. Rev. D* **62** (2000) 063511.
- [31] D. Boyanovsky, H. J. de Vega and N. G. Sanchez, *Constraints on dark matter particles from theory, galaxy observations, and N-body simulations*, *Phys. Rev. D* **77** (2008) 043518.
- [32] A. Boyarsky, O. Ruchayskiy and D. Iakubovskiy, *A lower bound on the mass of dark matter particles*, *J. Cosmol. Astropart. Phys.* **3** (2009) 5.

- [33] H. J. de Vega and N. G. Sanchez, *Model-independent analysis of dark matter points to a particle mass at the keV scale*, *Mon. Not. Roy. Astron. Soc.* **404** (2010) 885.
- [34] A. Macciò, S. Paduroiu, D. Anderhalden, A. Schneider, and B. Moore, *Cores in warm dark matter haloes: a Catch 22 problem*, *Mon. Not. Roy. Astron. Soc.* **424** (2012) 1105 (2012); *Erratum*, *Mon. Not. Roy. Astron. Soc.* **428** (2013) 3715.
- [35] M.R. Lovell, C.S. Frenk, V.R. Eke, A. Jenkins, L. Gao and T. Theuns, *et al.*, *The properties of warm dark matter haloes*, *Mon. Not. Roy. Astron. Soc.* **439** (2014) 300.
- [36] F. Villaescusa-Navarro and N. Dalal, *Cores and cusps in warm dark matter halos*, *JCAP* **03** (2011) 024.
- [37] C. Destri, H. J. de Vega and N. G. Sanchez, *Fermionic warm dark matter produces galaxy cores in the observed scales because of quantum mechanics*, *New Astron.* **22** (2013) 39.
- [38] C. Destri, H. J. de Vega and N. G. Sanchez, *Quantum WDM fermions and gravitation determine the observed galaxy structures*, *Astropart. Phys.* **46** (2013) 14.
- [39] J.F. Navarro, C.S. Frenk and S.D.M. White, *A Universal density profile from hierarchical clustering*, *Astrophys. J.* **490** (1997) 493.
- [40] J. Madsen, *Finite-mass isothermal spheres and the structure of globular clusters*, *Mon. Not. Roy. Astron. Soc.* **280** (1996) 1089.
- [41] L.L.R. Williams, J. Hjorth and R. Wojtak, *Statistical mechanics of collisionless orbits. III. Comparison with N-body simulations*, *Astrophys. J.* **725** (2010) 282.
- [42] C. Nolting, L.L.R. Williams, M. Boylan-Kolchin and J. Hjorth, *Testing DARKexp against energy and density distributions of Millennium-II halos*, *JCAP* **09** (2016) 042.
- [43] L.J. Beraldo e Silva, M. Lima and L. Sodré, *Testing phenomenological and theoretical models of dark matter density profiles with galaxy clusters*, *Mon. Not. Roy. Astron. Soc.* **436** (2013) 2616.
- [44] K. Umetsu, A. Zitrin, D. Gruen, J. Merten, M. Donahue and M. Postman, *CLASH: Joint Analysis of Strong-Lensing, Weak-Lensing Shear and Magnification Data for 20 Galaxy Clusters*, *Astrophys. J.* **821** (2016) 116.
- [45] L.L.R. Williams and J. Hjorth, *Statistical mechanics of collisionless orbits. II. Structure of halos*, *Astrophys. J.* **722** (2010) 856.
- [46] J. Binney, *The phase space structure of $r^{1/4}$ galaxies: Are these galaxies 'isothermal' after all?*, *Mon. Not. Roy. Astron. Soc.* **200** (1982) 951.
- [47] C. Destri, *Cored density profiles in the DARKexp model*, *JCAP* **05** (2018) 010.
- [48] L.L.R. Williams, J. Hjorth, R. Wojtak, *Statistical mechanics of collisionless orbits. IV. Distribution of angular momentum*, *Astrophys. J.* **783** (2014) 13.
- [49] J. Nocedal and S.J. Wright, *Numerical Optimization* 1999 Springer-Verlag New York,
- [50] T. A. Driscoll, N. Hale, and L. N. Trefethen, editors, *Chebfun Guide*, Pafnuty Publications, Oxford, 2014.